

# Complementarity-Free Multi-Contact Modeling and Optimization for Dexterous Manipulation

Wanxin Jin  
Arizona State University

[Video](#) [Code](#) [Email](#)

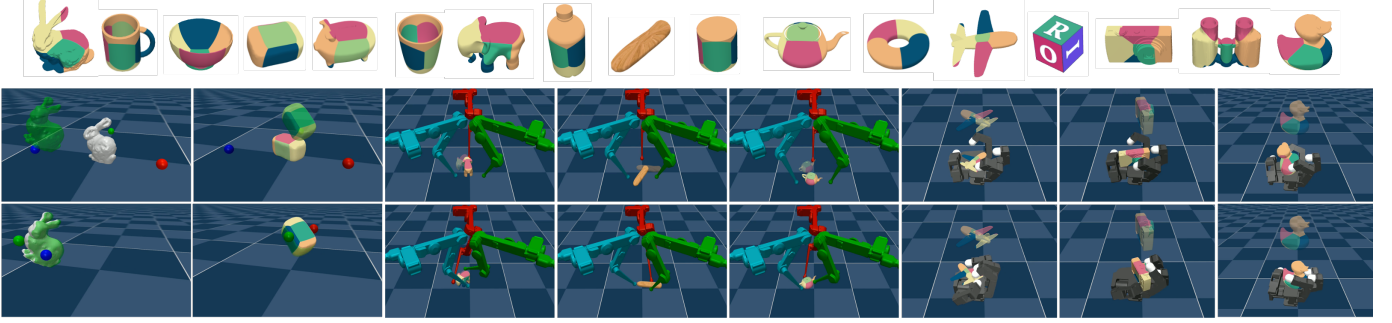


Fig. 1: We propose a complementarity-free multi-contact model that achieves state-of-the-art performance in planning and control across various challenging dexterous manipulation tasks, including fingertip in-air manipulation (cols. 1-2), TriFinger in-hand manipulation (cols. 3-5), and Allegro hand on-palm reorientation (cols. 6-8), all with diverse objects (first row). The second and third rows show the initial and final scenes of selected tasks, with the target object pose shown in transparency. Object diameters range from 50 [mm] to 150 [mm]. [Video link](#).

**Abstract**—A significant barrier preventing model-based methods from achieving real-time and versatile dexterous robotic manipulation is the inherent complexity of multi-contact dynamics. Traditionally formulated as complementarity models, multi-contact dynamics introduces non-smoothness and combinatorial complexity, complicating contact-rich planning and optimization. In this paper, we circumvent these challenges by introducing a lightweight yet capable multi-contact model. Our new model, derived from the duality of optimization-based contact models, dispenses with the complementarity constructs entirely, providing computational advantages such as closed-form time stepping, differentiability, automatic satisfaction with Coulomb’s friction law, and minimal hyperparameter tuning. We demonstrate the model’s effectiveness and efficiency for planning and control in a range of challenging dexterous manipulation tasks, including fingertip 3D in-air manipulation, TriFinger in-hand manipulation, and Allegro hand on-palm reorientation, all performed with diverse objects. Our method consistently achieves state-of-the-art results: (I) a 96.5% average success rate across all objects and tasks, (II) high manipulation accuracy with an average reorientation error of  $11^\circ$  and position error of 7.8mm, and (III) contact-implicit model predictive control running at 50-100 Hz for all objects and tasks. These results are achieved with minimal hyperparameter tuning.

## I. INTRODUCTION

Achieving real-time and versatile dexterity in robotic manipulation, which requires fast reasoning about frequent making and breaking contacts with various objects and physical environments, remains a significant challenge. Notable results have been delivered by reinforcement learning [1]–[4], albeit at the expense of extensive environment data, lengthy training process, and limited object generalizability. In contrast, progress in model-based planning and control methods been relatively slow, with existing methods typically limited to simple contact-less manipulation settings. A primary challenge for model-based methods is the non-smooth and hybrid nature of contact-rich dynamics — smooth motions are frequently interrupted by

discrete contact events (i.e., making or breaking contacts) [5], [6]. This introduces computational challenges in both learning of contact dynamics [7] and combinatorics optimization of contact modes [5], [8]. Recent work has made some headway, including new algorithms for learning hybrid dynamics [7], [9], differentiable contact modeling [10]–[12], multi-contact predictive control [13]–[16], and contact-rich planning [5], [8]. Despite these efforts, the computational challenges induced by non-smooth contact dynamics remain a significant barrier for model-based methods to achieve the real-time versatility needed for complex dexterous manipulation involving diverse object geometries and robot morphologies.

This paper seeks to advance the state-of-the-art in model-based dexterous manipulation by addressing a critical question: *Can we circumvent the computational challenges induced by the non-smooth multi-contact dynamics in the early stage of contact modeling?* Unlike existing efforts [5], [8], [13]–[16], we do NOT pursue abstract learning architectures [6], [17], propose artificial smoothing strategies for existing contact dynamics [10]–[12], nor develop planning algorithms that explicitly tackle the hybrid decision space. Instead, our contribution is a *new multi-contact model that overcomes the non-smooth and hybrid computational complexities via a physics modeling perspective*, enabling significant speed and performance improvement in model-based dexterous manipulation.

Specifically, unlike traditional complementarity-based formulations [10], [18]–[22] for modeling rigid-body contacts, our proposed method *modifies the complementarity constructs in the dual space of the optimization-based contact models* [19], [23] *into explicit forms*. This results in a new complementarity-free multi-contact model that has several computational advantages. (I) *Closed-form and differentiable time-stepping*: the next system state is a closed-form differentiable function of the current state and input, thus avoiding solving complementarity problems [24], optimization [23], or residual equations [10]

for contact constraint resolution. (II) *Automatic satisfaction with Coulomb's friction law in a single term*: the new model resolves the normal and frictional contact forces using a *single* term that automatically respects the Coulomb friction cone. This is unlike the contact models [25]–[28] that handle normal and frictional components independently, leading to additional hyperparameters. (III) *Fewer hyperparameters*: the proposed model has fewer parameters, making it easy to tune, and it also supports model auto-tuning using any learning framework.

The goal of the new contact model is not to compete with existing high-fidelity physics simulators [10], [18]–[22], but rather to offer a lightweight, smooth, yet capable surrogate that addresses the inherent computational challenges associated with existing complementarity-based models, particularly when used for contact-rich optimization and control. We integrate this model into model predictive control (MPC) framework for contact-implicit online planning and control. With minimal hyperparameter tuning, we achieve state-of-the-art performance across challenging dexterous manipulation tasks, including 3D in-air fingertip manipulation, TriFinger in-hand manipulation, and Allegro hand on-palm reorientation, all with diverse objects, as shown in Fig. 1. Our method sets a new benchmark for model-based contact-rich dexterous manipulation:

- Highly versatile dexterity: 96.5% average success rate across all objects and environments.
- High-accuracy dexterity: average object reorientation error of  $11^\circ$  and position error of 7.8mm.
- Real-time dexterity: contact-implicit MPC running at 50-100 Hz for all objects and robots.

## II. RELATED WORKS

### A. Rigid Body Multi-contact Models

1) *Nonconvex Complementarity Contact Models*: Rigid body contact dynamics is traditionally formulated using complementarity models [24], [29], [30]: it enforces no interpenetration and no contact force at a distance. The Coulomb friction law, which governs sticking and sliding contacts [24], [30], can also be expressed as complementarity constraints via the maximum dissipation principle [31], leading to a nonlinear complementarity problem (NCP). Since the NCPs cannot be interpreted as the KKT conditions of a convex program, they are challenging to solve. To simplify computation, Coulomb friction cones are often approximated by polyhedral cones [19], [30], converting the NCP into a linear complementarity problem (LCP) [30], for which mature solvers exist [32].

2) *Cone Complementarity Contact Models*: In [23], Anitescu proposed relaxing the NCP formulation, by constraining the contact velocity within a dual friction cone. Then, the NCP becomes cone complementarity problem (CCP), which attains computational benefits such as fast convergence and solution guarantees [33], [34]. A side effect of CCP is that it allows for small normal motion at the contact even when bodies should remain in contact. This creates a “boundary layer” whose size is proportional to time step and tangential velocity [33].

3) *Optimization-based Contact Models*: The CCP described above corresponds to the KKT optimality conditions of a convex optimization problem with second-order cone constraints [23]. This allows for the formulation of a primal convex optimization (with velocities as decision variables) or a dual optimization (with contact forces as decision variables). The primal approach has been used in work [5], [35], while the dual formulation is used in the MuJoCo simulator [19], albeit with a regularization term for model invertibility. The dual objective function can be interpreted as minimizing kinetic energy in contact frames.

4) *Differentiable Contact Models*: Several alternative models have been proposed to approximate complementarity-based models for differentiability. [25] introduced penalty functions to model contact normal and frictional forces. [10] proposes relaxing complementarity constraint, which in optimization-based model case, is equivalent to solving an unconstrained optimization with constraints penalized via log-barrier functions [36]. [37] proposed implicit complementarity, converting all constraints to unconstrained optimization with intermediate variables. [26], [38] developed penalty-based contact models. A shared feature is that those methods ultimately need to solve a residual equation for contact constraint resolution, and differentiability is obtained via implicit function theorem [39].

5) *Why is our model new?*: Two features distinguish the proposed model from existing ones. First, closed-form contact constraint resolution: our model builds on optimization-based contact dynamics [23], [35], but instead of solving the primal [23], [35] or dual programs [19], we approximate the complementarity constraints in the dual space with an explicit form (by contact decoupling). This approximation leads to a *closed-form* contact constraint resolution, eliminating the need to solve optimization [23], residual [10], or complementarity problems [24] at each time stepping.

Second, unified handling of contact normal and friction: while previous work [26]–[28], [38] has also explored closed-form contact dynamics models, our novelty, however, is that *our closed-form model is approximated in the dual friction cone*. This allows for the *unified* treatment of contact normal forces and frictional forces within a single term, ensuring automatic sanctification with Coulomb's friction law. In contrast, existing models [26]–[28], [38] treat the contact normal and enforce Coulomb's friction separately, which typically leads to additional hyperparameters and potential nonphysical artifacts.

### B. Planning and Control with Contact Dynamics

Planning and control for multi-contact systems are challenging because algorithms must determine when and where to make or break contacts, with complexity scaling exponentially with potential contact locations and planning horizons. Traditional methods [40], [41] predefine contact sequences, which could be possible for tasks like legged locomotion [42]. Modern approaches focus on contact-implicit planning [43], solving for both contact location and sequencing. Two main strategies are proposed. The first is to smooth contact transition boundaries. In [5], [16], [43], [44] complementarity constraints are relaxed. The other is to maintain the hybrid structures and cast the planning as mixed integer program, as done in [5], [13], [14], [45]–[47].

This paper develops the contact-implicit planning and control based on the proposed complementarity-free contact model. The resulting contact-implicit optimization can be readily solved using standard optimization techniques [48] or MPC tools [49], requiring no additional smoothing constructs or optimization programming effort. With its closed form and smooth nature, our model significantly improves the speed of online planning; e.g., our contact-implicit MPC controller runs up to 50-100 Hz in the Allegro Hand dexterous reorientation tasks.

### C. Reinforcement Learning for Dexterous Manipulation

Reinforcement learning (RL) has shown impressive results in dexterous manipulation [1]–[4]. For instance, [1], [3] employ model-free RL for in-hand object reorientation; [50] introduces an adaptive framework for reorienting various objects. However, these methods require millions to billions of environment samples. Model-based RL [6], [17] offers better efficiency, but unstructured deep models can struggle with multimodality [7], [17]. The prior work [6] shows incorporating hybrid constructs into models significantly improves efficiency, enabling dexterous manipulation with only thousands of environment samples.

RL has set the state-of-the-art in challenging dexterous manipulation tasks, e.g., TriFinger [3], [6] and Allegro hand manipulation [50], where model-based methods often struggle. Our proposed method aims to bridge this gap and even surpass state-of-the-art RL in success rate and manipulation accuracy.

## III. PRELIMINARY AND PROBLEM STATEMENT

We consider a manipulation system, comprised of an actuated robot, unactuated object and environment (e.g., ground). We define the following notations used in the rest of the paper.

$\mathbf{q}_o \in \mathbb{R}^{n_o}$	object position
$\mathbf{v}_o \in \mathbb{R}^{n_o}$	object velocity
$\boldsymbol{\tau}_o \in \mathbb{R}^{n_o}$	non-contact force applied to object
$\mathbf{q}_r \in \mathbb{R}^{n_r}$	robot position (generalized coordinate)
$\mathbf{v}_r \in \mathbb{R}^{n_r}$	robot velocity (generalized coordinate)
$\boldsymbol{\tau}_r \in \mathbb{R}^{n_r}$	non-contact force to robot
$\mathbf{u} \in \mathbb{R}^{n_u}$	control input applied to robot
$\mathbf{q}=(\mathbf{q}_o, \mathbf{q}_r)$	system position
$\mathbf{v}=(\mathbf{v}_o, \mathbf{v}_r)$	system velocity
$\boldsymbol{\lambda}=(\boldsymbol{\lambda}^n, \boldsymbol{\lambda}^d)$	contact impulse/force (normal, friction)
$\mathbf{J}_r$	contact Jacobian of the robot
$\mathbf{J}_o$	contact Jacobian of the object
$\mathbf{J}=[\mathbf{J}_o, \mathbf{J}_r]$	contact Jacobian of the system
$\mathbf{J}=[\mathbf{J}^n; \mathbf{J}^d]$	$\mathbf{J}$ reformatted in normal & tangential
$\mathbf{J}^d=[\mathbf{J}_1^d; \dots; \mathbf{J}_{n_d}^d]$	tangential Jacobian for polyhedral cone

### A. Optimization-based Quasi-Dynamic Contact Model

For simplicity, we model a manipulation system using the quasi-dynamic formulation [5], [8], [46], [51], which primarily captures the positional displacement of a contact-rich system in relation to contact interactions and inputs, while ignoring the inertial and Coriolis forces that are less significant under less dynamic motion. Quasi-dynamic models benefit from simplicity and suffice for a wide variety of manipulation tasks [5], [8], [46]. It should be noted our following model can be readily

extended to full dynamic model, which will be shown in Section VI-B.

Formally, consider a manipulation system with  $n_c$  potential contacts, which could happen between the robot and object or/and between object and the environment. The time-stepping equation of the quasi-dynamic model is

$$\begin{aligned} \epsilon \mathbf{M}_o \mathbf{v}_o &= h \boldsymbol{\tau}_o + \sum_{i=1}^{n_c} \mathbf{J}_{o,i}^\top \boldsymbol{\lambda}_i, \\ h \mathbf{K}_r (h \mathbf{v}_r - \mathbf{u}) &= h \boldsymbol{\tau}_r + \sum_{i=1}^{n_c} \mathbf{J}_{r,i}^\top \boldsymbol{\lambda}_i. \end{aligned} \quad (1)$$

Here,  $h$  is the time step. The first equation is the motion of the object with  $\epsilon \mathbf{M}_o \in \mathbb{R}^{n_o \times n_o}$  the regularized mass matrix for the object ( $\epsilon > 0$  is the regularization parameter) [52]. The second equation is the motion of the robot, where we follow [35] and consider the robot is in impedance control [53] and thus can be viewed as a "spring" with stiffness  $\mathbf{K}_r \in \mathbb{R}^{n_r \times n_r}$ ; the input  $\mathbf{u} \in \mathbb{R}^{n_r}$  to the robot is the *desired joint displacement*.  $\boldsymbol{\lambda}_i = (\lambda_i^n, \boldsymbol{\lambda}_i^d) \in \mathbb{R}^3$  is the  $i$ -th contact impulse, with contact normal component  $\lambda_i^n$  and frictional component  $\boldsymbol{\lambda}_i^d$ .

Next, we add contact constraints between the contact impulse and system motion using the cone complementarity formulation proposed by Anitescu in [23], [33]. Specifically, the cone complementarity constraint at contact  $i$  writes

$$\mathcal{K}_i \ni \boldsymbol{\lambda}_i \perp \mathbf{J}_i \mathbf{v} + \frac{1}{h} \begin{bmatrix} \phi_i \\ 0 \\ 0 \end{bmatrix} \in \mathcal{K}_i^*, \quad \forall i = \{1, \dots, n_c\}, \quad (2)$$

where  $\phi_i$  is the normal distance at contact  $i$ ;  $\mathcal{K}_i$  is the Coulomb frictional cone, defined as  $\mathcal{K}_i = \{\boldsymbol{\lambda}_i \in \mathbb{R}^3 \mid \mu_i \lambda_i^n \geq \|\boldsymbol{\lambda}_i^d\|\}$ ;  $\mathcal{K}_i^*$  is the dual cone to  $\mathcal{K}_i$ , and the right side of (2) says that at contact  $i$ , the relaxed contact velocity has to lie in  $\mathcal{K}_i^*$ , i.e.,

$$\mathbf{v} \in \left\{ \mathbf{v} \mid \mathbf{J}_i^n \mathbf{v} + \frac{\phi_i}{h} \geq \mu_i \|\mathbf{J}_i^d \mathbf{v}\| \right\}, \quad (3)$$

with  $\mu_i$  the friction coefficient for contact  $i$ .

In [23], Anitescu showed (1) and (2) are the KKT optimality conditions for the following primal optimization [23]:

$$\begin{aligned} \min_{\mathbf{v}} \quad & \frac{1}{2} h^2 \mathbf{v}^\top \mathbf{Q} \mathbf{v} - h \mathbf{v}^\top \mathbf{b}(\mathbf{u}) \\ \text{subject to} \quad & \mathbf{J}_i \mathbf{v} + \frac{1}{h} \begin{bmatrix} \phi_i \\ 0 \\ 0 \end{bmatrix} \in \mathcal{K}_i^*, \quad i \in \{1 \dots n_c\}, \end{aligned} \quad (4)$$

where  $\mathbf{Q} \in \mathbb{R}^{(n_o+n_r) \times (n_o+n_r)}$  and  $\mathbf{b}(\mathbf{u}) \in \mathbb{R}^{n_o+n_r}$  are

$$\mathbf{Q} := \begin{bmatrix} \epsilon \mathbf{M}_o / h^2 & \mathbf{0} \\ \mathbf{0} & \mathbf{K}_r \end{bmatrix}, \quad \mathbf{b}(\mathbf{u}) := \begin{bmatrix} \boldsymbol{\tau}_o \\ \mathbf{K}_r \mathbf{u} + \boldsymbol{\tau}_r \end{bmatrix}, \quad (5)$$

respectively. (4) is a second-order cone program (SOCP). To facilitate solving the SOCP, one can approximate it with a quadratic program (QP) by linearizing the second-order dual cone constraint using its polyhedral approximation [29]. Specifically, at contact  $i$ , one can use a symmetric set of  $n_d$  unit directional vectors  $\{\mathbf{d}_{i,1}, \mathbf{d}_{i,2}, \dots, \mathbf{d}_{i,n_d}\}$  to span the contact tangential plane [24], yielding the linearization of (3):

$$\mathbf{J}_i^n \mathbf{v} + \frac{\phi_i}{h} \geq \mu_i \mathbf{J}_{i,j}^d \mathbf{v}, \quad \forall j \in \{1 \dots n_d\} \quad (6)$$



with  $\mathbf{J}_{i,j}^d$  being the system Jacobian to the unit directional vector  $\mathbf{d}_j$  in the tangential plane of contact  $i$ . Hence, the SOCP in (4) can be simplified as the following QP

$$\begin{aligned} \min_{\mathbf{v}} \quad & \frac{1}{2} h^2 \mathbf{v}^\top \mathbf{Q} \mathbf{v} - h \mathbf{v}^\top \mathbf{b}(\mathbf{u}) \\ \text{subject to} \quad & (\mathbf{J}_i^n - \mu_i \mathbf{J}_{i,j}^d) \mathbf{v} + \frac{\phi_i}{h} \geq 0, \\ & i \in \{1 \dots n_c\}, j \in \{1 \dots n_d\}. \end{aligned} \quad (7)$$

In time-stepping prediction, Jacobians  $\mathbf{J}_i^n$  and  $\mathbf{J}_{i,j}^d$  are calculated from a collision detection routine [54] at the system's current position  $\mathbf{q}$ . The solution  $\mathbf{v}^+$  to (7) will be used to integrate from  $\mathbf{q}$  to the next position  $\mathbf{q}^+$ , and we simply write it as  $\mathbf{q}^+ = \mathbf{q} \oplus h \mathbf{v}^+$  ( $\oplus$  can involve quaternion integration).

### B. Model Predictive Control

The generic formulation of model predictive control is

$$\begin{aligned} \min_{\mathbf{u}_{0:T-1} \in [\mathbf{u}_{lb}, \mathbf{u}_{ub}]} \quad & \sum_{t=0}^{T-1} c(\mathbf{q}_t, \mathbf{u}_t) + V(\mathbf{q}_T) \\ \text{subject to} \quad & \mathbf{q}_{t+1} = \mathbf{f}(\mathbf{q}_t, \mathbf{u}_t), \quad t = 0, \dots, T-1, \\ & \text{given } \mathbf{q}_0. \end{aligned} \quad (8)$$

where model  $\mathbf{f}$  predicts the next system state. With  $\mathbf{q}_0$ , (8) searches for the optimal input sequence ( $\mathbf{u}_{lb}$  and  $\mathbf{u}_{ub}$  are control bounds), by minimizing the path  $c(\cdot)$  and final cost  $V(\cdot)$ .

In a manipulation system, the MPC policy is implemented in a receding horizon fashion, by repeatedly solving (8) at the real system state  $\mathbf{q}_k^{\text{real}}$  encountered at the policy rollout step  $k$  and only applying the first optimal input to the real system. Specifically, at the encountered system state  $\mathbf{q}_k^{\text{real}}$ , the MPC policy sets  $\mathbf{q}_0 = \mathbf{q}_k^{\text{real}}$  and solves (8). Only the first optimal input  $\mathbf{u}_0^*(\mathbf{q}_k^{\text{real}})$  is applied to the real system, evolving the system state to the next  $\mathbf{q}_{k+1}^{\text{real}}$ . This implementation creates a closed-loop control effect on the real system, i.e., feedback from system state  $\mathbf{q}_k^{\text{real}}$  to control input  $\mathbf{u}_0^*(\mathbf{q}_k^{\text{real}})$ .

### C. Problem: Contact-implicit MPC for Dexterous Manipulation

We are interested in real-time, contact-implicit MPC for dexterous manipulation. Directly using the QP-based contact model (7) in MPC (8) leads to a nested optimization, which is difficult to solve due to the non-smooth behavior of the contact model (7), i.e., the prediction "jumps" at the transitions between separate, sliding, and sticking contact modes. The goal of the paper is to develop a new surrogate multi-contact model  $\mathbf{f}$  in (8) to overcome the above challenges, enabling real-time and high-performance MPC for dexterous manipulation tasks.

## IV. COMPLEMENTARITY-FREE MULTI-CONTACT MODEL

### A. Duality of Optimization-based Contact Model

We proceed by establishing the dual problem of the QP-based contact model (7). First, define the shorthand notations:

$$\tilde{\mathbf{J}} := \begin{bmatrix} \mathbf{J}_1^n - \mu_1 \mathbf{J}_{1,1}^d \\ \vdots \\ \mathbf{J}_1^n - \mu_1 \mathbf{J}_{1,n_d}^d \\ \vdots \\ \mathbf{J}_{n_c}^n - \mu_{n_c} \mathbf{J}_{n_c,1}^d \\ \vdots \\ \mathbf{J}_{n_c}^n - \mu_{n_c} \mathbf{J}_{n_c,n_d}^d \end{bmatrix}, \quad \tilde{\boldsymbol{\phi}} := \begin{bmatrix} \phi_1 \\ \vdots \\ \phi_1 \\ \vdots \\ \phi_{n_c} \\ \vdots \\ \phi_{n_c} \end{bmatrix}, \quad \boldsymbol{\beta} := \begin{bmatrix} \beta_{1,1} \\ \vdots \\ \beta_{1,n_d} \\ \vdots \\ \beta_{n_c,1} \\ \vdots \\ \beta_{n_c,n_d} \end{bmatrix} \quad (9)$$

of dimension  $\tilde{\mathbf{J}} \in \mathbb{R}^{n_c n_d \times (n_o + n_r)}$ ,  $\tilde{\boldsymbol{\phi}} \in \mathbb{R}^{n_c n_d}$ , and  $\boldsymbol{\beta} \in \mathbb{R}^{n_c n_d}$ . Here,  $\boldsymbol{\beta}$  is the stacked vector of the dual variables for the  $n_c n_d$  constraints in (7). From convex optimization [55], it can be shown that the dual problem of (7) is

$$\max_{\boldsymbol{\beta} \geq 0} \quad -\frac{1}{2h^2} (h\mathbf{b} + \tilde{\mathbf{J}}^\top \boldsymbol{\beta})^\top \mathbf{Q}^{-1} (h\mathbf{b} + \tilde{\mathbf{J}}^\top \boldsymbol{\beta}) - \frac{1}{h} \tilde{\boldsymbol{\phi}}^\top \boldsymbol{\beta}. \quad (10)$$

The optimal primal solution  $\mathbf{v}^+$  to (7) and the dual solution  $\boldsymbol{\beta}^+$  to (10) has the following relationship

$$\mathbf{v}^+ = \frac{1}{h^2} \mathbf{Q}^{-1} (h\mathbf{b} + \tilde{\mathbf{J}}^\top \boldsymbol{\beta}^+). \quad (11)$$

As pointed out in [19], the dual optimization (10) can be physically interpreted as finding the contact impulse  $\boldsymbol{\beta}$  that minimizes the kinetic energy in contact frame:  $\frac{1}{2} \mathbf{v}^{+\top} (h^2 \mathbf{Q}) \mathbf{v}^+ + \frac{1}{h} \tilde{\boldsymbol{\phi}}^\top \boldsymbol{\beta}$ .

It is noted that the dual solution to (10) is not unique because the quadratic matrix  $\tilde{\mathbf{J}} \mathbf{Q}^{-1} \tilde{\mathbf{J}}^\top$  is not necessarily of full rank. In MuJoCo [19], to guarantee the invertibility of the contact model, i.e., the uniqueness of the contact force  $\boldsymbol{\beta}$ , it adds a small regularization term  $\mathbf{R}$  to the quadratic matrix, turning (10) into a strongly concave program

$$\begin{aligned} \max_{\boldsymbol{\beta} \geq 0} \quad & -\frac{1}{2h^2} \boldsymbol{\beta}^\top (\tilde{\mathbf{J}} \mathbf{Q}^{-1} \tilde{\mathbf{J}}^\top + \mathbf{R}) \boldsymbol{\beta} \\ & - \frac{1}{h} (\tilde{\mathbf{J}} \mathbf{Q}^{-1} \mathbf{b} + \tilde{\boldsymbol{\phi}})^\top \boldsymbol{\beta} - \frac{1}{2} \mathbf{b}^\top \mathbf{Q}^{-1} \mathbf{b}. \end{aligned} \quad (12)$$

where  $\mathbf{R} \in \mathbb{R}^{n_c n_d \times n_c n_d}$  is a diagonal regularization matrix with positive entries. The following lemma states the optimality condition for the regularized dual problem (12).

**Lemma 1.** *The dual solution to the regularized dual problem (12) satisfies the following dual complementarity constraints:*

$$\mathbf{0} \leq \boldsymbol{\beta} \perp \left( \tilde{\mathbf{J}} \mathbf{Q}^{-1} \tilde{\mathbf{J}}^\top + \mathbf{R} \right) \boldsymbol{\beta} + \left( \tilde{\mathbf{J}} \mathbf{Q}^{-1} \mathbf{b} + \tilde{\boldsymbol{\phi}} \right) \geq \mathbf{0}. \quad (13)$$

The proof of Lemma 1 is in Appendix. This lemma indicates solving (12) involves managing complementarity constraints.

### B. New Complementarity-Free Multi-Contact Model

To circumvent the dual complementarity in (13), we propose a new contact model based on Lemma 1. Assume, for now, the inverse of the first matrix on the right side of (13) can be replaced by a positive definite diagonal matrix  $\mathbf{K}(\mathbf{q}) \in \mathbb{R}^{n_c n_d \times n_c n_d}$ , i.e.,

$$\mathbf{K}(\mathbf{q}) \approx (\tilde{\mathbf{J}} \mathbf{Q}^{-1} \tilde{\mathbf{J}}^\top + \mathbf{R})^{-1}. \quad (14)$$

We will provide the physical justification for this assumption in the next subsection. The following lemma states a closed-form solution to the dual complementarity (13) with the replacement in (14).

**Lemma 2.** *Let a positive definite diagonal matrix  $\mathbf{K}(\mathbf{q})$  replace  $(\tilde{\mathbf{J}} \mathbf{Q}^{-1} \tilde{\mathbf{J}}^\top + \mathbf{R})^{-1}$  as in (14). The dual complementarity (13) then has a closed-form solution:*

$$\boldsymbol{\beta}^+ = \max \left( -h \mathbf{K}(\mathbf{q}) (\tilde{\mathbf{J}} \mathbf{Q}^{-1} \mathbf{b} + \tilde{\boldsymbol{\phi}}), \mathbf{0} \right). \quad (15)$$

Furthermore, the approximate primal solution to (7) is

$$\mathbf{v}^+ = \frac{1}{h} \mathbf{Q}^{-1} \mathbf{b} + \frac{1}{h} \mathbf{Q}^{-1} \tilde{\mathbf{J}}^\top \max \left( -\mathbf{K}(\mathbf{q}) (\tilde{\mathbf{J}} \mathbf{Q}^{-1} \mathbf{b} + \tilde{\boldsymbol{\phi}}), \mathbf{0} \right). \quad (16)$$



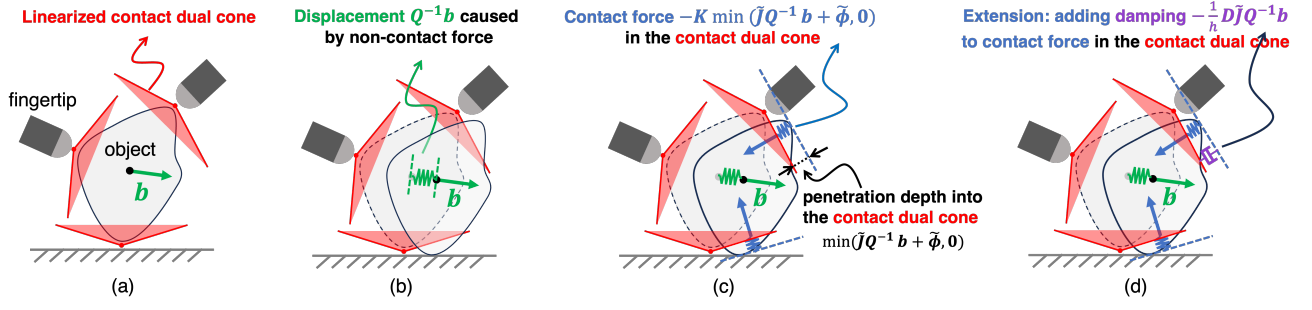


Fig. 2: The physical interpretation of the proposed complementarity-free multi-contact model (16) using a 2D fingertip manipulation example. (a) The dual cone constraints, depicted by red shaded areas, between the object and the ground and fingertips. (b) The displacement (green) caused solely by the non-contact force  $\mathbf{b}$  applied to the system to move the object from dashed position to solid position. (c) The spring-like contact force (blue) resulting from the penetration (black) of the contact dual cone. (d) An extension: a damping effect (purple) is added to the contact force term.

The proof of Lemma 2 is given in Appendix. Lemma 2 presents an important result: by substituting  $(\tilde{\mathbf{J}}\mathbf{Q}^{-1}\tilde{\mathbf{J}}^T + \mathbf{R})^{-1}$  with a positive diagonal matrix  $\mathbf{K}(\mathbf{q})$ , the complementarity constraints in the original dual condition (13) are eliminated. Critically, this substitution makes the contact time-stepping prediction (16) have closed-form solution and free from complementarity. We thus name (16) the *complementarity-free multi-contact model*. Although the above treatment can cause the time-stepping prediction  $\mathbf{v}^+$  in (16) to differ from the true primal solution of the original QP-based contact model (7), it offers significant computational benefits, particularly for model-based multi-contact optimization, as will be shown later. In fact,  $\mathbf{K}(\mathbf{q})$  has an intuitive physical interpretation, which will be discussed in the next subsection.

While our complementarity-free time stepping (16) approximates (7), we do not expect the resolved velocity  $\mathbf{v}^+$  to strictly satisfy the original dual cone constraints in (7)—although it can potentially achieve so by appropriately choosing the matrix  $\mathbf{K}(\mathbf{q})$ . In fact, relaxing the dual cone constraint in (7) provides our model (16) with unique advantages that are not available in (7), particularly in mitigating the non-physical artifacts with (7) (or general Anitescu models [23], [33]), as we elaborate in the next subsection and later experiments in Section VI-B.

### C. Physical Interpretation of the New Model

We next provide the physical interpretation of the new complementarity-free multi-contact model (16) using a 2D fingertip manipulation example in Fig. 2. First, recall the linearized dual cone constraints (6) in the original QP-based contact model (7). Using (9), we can compactly express these dual cone constraints as

$$h\tilde{\mathbf{J}}\mathbf{v} + \tilde{\boldsymbol{\phi}} \geq \mathbf{0}. \quad (17)$$

In Fig. 2(a)-(d), the contact dual cone constraints are shown in red areas.

Now, returning to the proposed model (16), we multiply the time step  $h$  on both sides of (16), leading to

$$h\mathbf{v}^+ = \mathbf{Q}^{-1} \left( \underbrace{\mathbf{b} + \tilde{\mathbf{J}}^T \overbrace{\max(-\mathbf{K}(\tilde{\mathbf{J}}\mathbf{Q}^{-1}\mathbf{b} + \tilde{\boldsymbol{\phi}}), \mathbf{0})}^{\text{contact force in contact dual cone}}}_{\text{total force in generalized coordinate}} \right). \quad (18)$$

Equation (18) shows that the proposed model (16) can be interpreted as a force-spring system, where  $h\mathbf{v}^+$  represents the position displacement in the generalized coordinate, and the right side accounts for the total force applied to the system. The matrix  $\mathbf{Q}$ , defined in (5), encodes the system's spring stiffness in response to the total force. The total force consists of two components: (i) the non-contact force  $\mathbf{b}$  (e.g., gravity and actuation forces), shown in green arrows in Fig. 2, and (ii) the contact force  $\boldsymbol{\lambda}_{\text{contact}} := \max(-\mathbf{K}(\tilde{\mathbf{J}}\mathbf{Q}^{-1}\mathbf{b} + \tilde{\boldsymbol{\phi}}), \mathbf{0})$ , shown in blue arrows in Fig. 2(c), applied within the contact dual cone and then converted to  $\tilde{\mathbf{J}}^T \boldsymbol{\lambda}_{\text{contact}}$  in the generalized coordinate. Without contact forces, the system displacement would be  $\mathbf{Q}^{-1}\mathbf{b}$ , as shown in Fig. 2(b)-(d) from the dashed object positions to the solid object positions.

By examining the contact force  $\boldsymbol{\lambda}_{\text{contact}}$  in (18) and combining the contact dual cone constraint in (17), we have

$$\boldsymbol{\lambda}_{\text{contact}} = -\mathbf{K} \underbrace{\min(\tilde{\mathbf{J}}\mathbf{Q}^{-1}\mathbf{b} + \tilde{\boldsymbol{\phi}}, \mathbf{0})}_{\substack{\text{penetration depth into the contact dual cone (17)} \\ \text{due to the displacement } \mathbf{Q}^{-1}\mathbf{b} \text{ caused by non-contact force } \mathbf{b}}}. \quad (19)$$

Thus, the contact force  $\boldsymbol{\lambda}_{\text{contact}}$  also behaves like a spring force, proportional to the penetration depth into the contact dual cone,  $\min(\tilde{\mathbf{J}}\mathbf{Q}^{-1}\mathbf{b} + \tilde{\boldsymbol{\phi}}, \mathbf{0})$ , which is caused by the displacement  $\mathbf{Q}^{-1}\mathbf{b}$  from the non-contact force  $\mathbf{b}$ . This has been shown in black arrows in Fig. 2(c). Notably, the matrix  $\mathbf{K}(\mathbf{q})$  introduced in Lemma 2 represents the *stiffness of the contact dual cone*. This is illustrated in blue in Fig. 2(c).

As analyzed above, our complementarity-free contact model (16) actually leverages the penetration/violation of the dual cone constraints (17) (also see Fig. 2(c-d)) to generate spring-like contact force. Thus, (16) has relaxed the dual cone constraints. In fact, the dual cone constraints in (7) are more a mathematical convenience than physical phenomenon (although [23], [33] provide a microscopic physical interpretation). Strictly enforcing the dual cone constraints will introduce non-physical artifacts (e.g., boundary layer effect), compared to non-convex complementary models (NCP/LCP) [24], [29], [30]. By relaxation of dual cone constraints, our model (16) will reduce such artifacts, as we will show in the later experiments in Section VI-B.

#### D. Property and Differentiability of the New Model

1) *Automatic satisfaction of Coulomb's Friction Law:* (19) and (15) indicate  $h\tilde{\mathbf{J}}^\top \boldsymbol{\lambda}_{\text{contact}} = \tilde{\mathbf{J}}^\top \boldsymbol{\beta}^+$ . Extending the right side based on the definitions (9) leads to

$$h\tilde{\mathbf{J}}^\top \boldsymbol{\lambda}_{\text{contact}} = \sum_{i=1}^{n_c} \left( \mathbf{J}_i^{n\top} \sum_{j=1}^{n_d} \beta_{i,j}^+ + \mu_i \sum_{j=1}^{n_d} \mathbf{J}_{i,j}^{d\top} \beta_{i,j}^+ \right). \quad (20)$$

From (20), one can see that at the contact location  $i$ , the contact impulse  $h\boldsymbol{\lambda}_{i,\text{contact}}$  can be decomposed into

$$\begin{aligned} \text{normal force: } h\boldsymbol{\lambda}_{i,\text{contact}}^n &:= \left( \sum_{j=1}^{n_d} \beta_{i,j}^+ \right) \mathbf{n}_i, \\ \text{frictional force: } h\boldsymbol{\lambda}_{i,\text{contact}}^d &:= \mu_i \sum_{j=1}^{n_d} \beta_{i,j}^+ \mathbf{d}_{i,j}. \end{aligned} \quad (21)$$

By the triangle inequality,  $\mu_i \|\boldsymbol{\lambda}_{i,\text{contact}}^d\| \geq \|\boldsymbol{\lambda}_{i,\text{contact}}^d\|$  follows. Thus, the contact force  $\boldsymbol{\lambda}_{\text{contact}}$  (18) or (19) in the proposed model (16) automatically satisfies the Coulomb friction law.

2) *Differentiability:* The proposed complementarity-free model (16) is not differentiable due to max operation. One thus can replace max operation with smooth **SoftPlus** function

$$\text{SoftPlus}(x) = \ln(1 + e^{\gamma x}) / \gamma \quad \text{with } \gamma > 0, \quad (22)$$

with  $\gamma$  controlling its accuracy to  $\max(x, 0)$ . Thus, a differentiable version of the complementarity-free model (16) is

$$\mathbf{v}^+ = \frac{1}{h} \mathbf{Q}^{-1} \mathbf{b} + \frac{1}{h} \mathbf{Q}^{-1} \tilde{\mathbf{J}}^\top \text{SoftPlus} \left( -\mathbf{K}(\mathbf{q})(\tilde{\mathbf{J}} \mathbf{Q}^{-1} \mathbf{b} + \tilde{\boldsymbol{\phi}}) \right). \quad (23)$$

#### E. Extension to Dynamic Settings

Since the contact force  $\boldsymbol{\lambda}_{\text{contact}}$  in (18) is a spring-like force, a natural extension is to include a damping term to stabilize the contact resolution, as shown in Fig. 2(d), i.e.,

$$\boldsymbol{\lambda}_{\text{contact}}^{\text{ext}} := \max \left( -\mathbf{K}(\mathbf{q})(\tilde{\mathbf{J}} \mathbf{Q}^{-1} \mathbf{b} + \tilde{\boldsymbol{\phi}}) - \underbrace{\mathbf{D}(\mathbf{q}) \tilde{\mathbf{J}} (\mathbf{Q}^{-1} \mathbf{b} / h)}_{\text{damping term}}, 0 \right) \quad (24)$$

where  $\mathbf{D}(\mathbf{q})$  is a diagonal damping matrix, and  $\frac{1}{h} \mathbf{Q}^{-1} \mathbf{b}$  is the velocity at the contact frame caused by the non-contact force  $\mathbf{b}$ . Consequently, the extended complementarity-free multi-contact model becomes

$$\mathbf{v}^+ = \frac{1}{h} \mathbf{Q}^{-1} \mathbf{b} + \frac{1}{h} \mathbf{Q}^{-1} \tilde{\mathbf{J}}^\top \boldsymbol{\lambda}_{\text{contact}}^{\text{ext}}. \quad (25)$$

This extension can be less significant in quasi-dynamic systems, because the velocities are small. However, it plays a significant role in stabilizing contact resolution in dynamic simulation. In Section VI-B, we will demonstrate the behavior of the contact simulation of (25) in dynamic scenarios. A comprehensive investigation of the full dynamic complementarity-free multi-contact model, however, is left for future work.

#### V. COMPLEMENTARITY-FREE CONTACT-IMPLICIT MPC

With the proposed complementarity-free multi-contact model, the MPC formulation (8) becomes

$$\begin{aligned} \min_{\mathbf{u}_0: T-1 \in [\mathbf{u}_b, \mathbf{u}_{ub}]} \quad & \sum_{t=0}^{T-1} c(\mathbf{q}_t, \mathbf{u}_t) + V(\mathbf{q}_T) \\ \text{subject to} \quad & \mathbf{q}_{t+1} = \mathbf{q}_t \oplus h\mathbf{v}_t^+, \quad t = 0, \dots, T-1 \\ & \mathbf{v}_t^+ \text{ is (23) with } \tilde{\mathbf{J}} \text{ and } \tilde{\boldsymbol{\phi}}, \text{ given } \mathbf{q}_0. \end{aligned} \quad (26)$$

where  $\oplus$  is the integration of system position with velocity.

In (26), at each prediction step  $t$ , the contact Jacobian  $\tilde{\mathbf{J}}(\mathbf{q}_t)$  and collision distance  $\tilde{\boldsymbol{\phi}}(\mathbf{q}_t)$  should ideally be computed for the predicted state  $\mathbf{q}_t$  using a collision detection routine [54]. However, including the collision detection operation inside the MPC optimization (26) is challenging due to its non-differentiability. Fortunately, in a receding horizon framework, one can do once collision detection for each encountered real-system state  $\mathbf{q}_0 = \mathbf{q}_k^{\text{real}}$  to obtain  $\tilde{\mathbf{J}}(\mathbf{q}_0)$  and  $\tilde{\boldsymbol{\phi}}(\mathbf{q}_0)$ , which then remain fixed inside the MPC prediction. This is equivalent to linearizing the contact geometry, which works well for short-horizon MPC (i.e.,  $T$  is small). We summarize the complementarity-free contact-implicit MPC in Algorithm 1.

---

#### Algorithm 1: Complementarity-free contact-implicit MPC

---

**Initialization:** Hyperparameter  $\mathbf{K}$  for the model (23)  
**for** MPC rollout step  $k = 0, 1, 2, \dots$  **do**  
     Get current system position  $\mathbf{q}_k^{\text{real}} = \text{env.get\_qpos}()$ ;  
     Collision detection to calculate  $\tilde{\mathbf{J}}(\mathbf{q}_k^{\text{real}})$  and  $\tilde{\boldsymbol{\phi}}(\mathbf{q}_k^{\text{real}})$ ;  
     Solve MPC (26) using any nonlinear optimization solver,  
     with  $\mathbf{q}_0 = \mathbf{q}_k^{\text{real}}$ ,  $\tilde{\mathbf{J}} = \tilde{\mathbf{J}}(\mathbf{q}_k^{\text{real}})$  and  $\tilde{\boldsymbol{\phi}} = \tilde{\boldsymbol{\phi}}(\mathbf{q}_k^{\text{real}})$ ;  
     Apply the first optimal input:  $\text{env.step}(\mathbf{u}_0^*(\mathbf{q}_k^{\text{real}}))$ ;  
**end**

---

In our implementation below, we will show that a constant diagonal matrix  $\mathbf{K}(\mathbf{q})$  surprisingly suffices for all the dexterous manipulation tasks (with different objects) we have encountered. A discussion on the setting of  $\mathbf{K}(\mathbf{q})$  is provided later. For the other model parameters, such as  $\epsilon$  for the object mass regularization in the quasi-dynamic model (1), we follow [5].  $\gamma = 100$  in **SoftPlus**, and  $n_d = 4$  in polyhedral frictional cone. We use the collision detection routine in MuJoCo [19], which implements [56], and solve the nonlinear MPC optimization using CasADi [57] with the IPOPT solver [58]. The following experiment results are reproducible using the code at <https://github.com/asu-iris/Complementarity-Free-Dexterous-Manipulation>, and video demos are available at <https://youtu.be/NsL4hbSXvFg>.

#### VI. CONTACT SIMULATION AND COMPARISON

##### A. Quasi-Dynamic Setting

We first test the performance of the complementarity-free model in predicting a contact-rich pushing-box scene in quasi-dynamic setting, shown in Fig. 3. In this setup, a bar with a linear joint (moving left-right), actuated by a low-level position controller, pushes varying numbers of cubes on a frictional ground. We compare the proposed model (23) with QP-based model (7). Since no true quasi-dynamic model exists for benchmarking, the comparison is primarily visual, with the metric being the timing for time-stepping calculation. The model settings are in Table I.

Although in the proposed model (23),  $\mathbf{K}(\mathbf{q})$  is configuration-dependant, we here and in the sequel simply set it as diagonal matrix with identical entries. Our later experiments show that this setting is sufficient for decent contact-rich prediction. Further discussion on setting  $\mathbf{K}(\mathbf{q})$  is provided later. The

TABLE I: System and parameter setting

Parameter	Proposed model (23)	QP-based model (7)
$\mathbf{q} \in \mathbb{R}^{7n_{\text{cube}}+1}$	poses of all cubes and pusher bar (robot) x position	
$\mathbf{u} \in \mathbb{R}$	desired bar displacement, sent to low-level controller	
$h$	0.02 [s]	
$\epsilon$	40	
$\mathbf{K}_r$	500	
$\mathbf{K}(\mathbf{q})$	$\mathbf{I}$	NA

QP-based contact model (7) uses OSQP solver [59] for time-stepping. For both models, we initialize the environment with the same random  $\mathbf{q}_0$  and set the same input  $\mathbf{u}_t = -0.001$ . The prediction horizon is  $T = 1000$  steps. The predicted scenes of pushing 10 boxes at different time steps are shown in Fig. 3(a). To compare the timing of one-step prediction, we varied the number of cubes  $n_{\text{cube}}$ , and the results are given in Fig. 3(b).

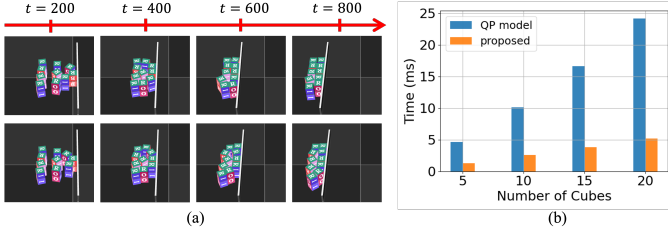


Fig. 3: (a) The predicted scene of pushing 10 boxes at different steps, by the proposed model (upper row) and QP-based model (bottom row). (b) Timing comparison for one-step prediction. The tests were conducted on a machine with an Apple M2 Pro chip.

Visually, Fig. 3(a) shows that the proposed model and the QP-based model yield similar predictions. However, Fig. 3(b) shows that the proposed model is 5x faster in one-step prediction. This is expected as the proposed model has an explicit time-stepping formulation, unlike the QP-based contact model, which requires solving a quadratic program at each time step.

### B. Full Dynamic Setting

Next, we will evaluate the simulation performance of the extended complementarity-free contact model (25) in full dynamic settings, and compare it against several baselines, including classical complementarity-based multi-contact models, a naive QP-based model (7) (in the dynamic form), and the MuJoCo simulator [19]. We will demonstrate that the proposed model: (I) mitigates non-physical artifacts commonly observed in QP models (7) and in general Anitescu's contact models such as the CCP [33] and Convex [23] models, due to the relaxation of dual cone constraints; and (II) achieves sufficient smoothness in contact dynamics due to the spring-damper-based contact resolution (25). Evaluation is conducted in three task settings.

In all dynamic settings below, instead of using the quasi-dynamic model (1), we employ the full dynamic model with current system position  $\mathbf{q}$  and velocity  $\mathbf{v}$ :

$$\mathbf{M}(\mathbf{q})\mathbf{v}^+ - \mathbf{M}(\mathbf{q})\mathbf{v} = h\boldsymbol{\tau}(\mathbf{q}, \mathbf{v}) + \sum_{i=1}^{n_c} \mathbf{J}^\top \boldsymbol{\lambda}_i, \quad (27)$$

where  $\mathbf{M}(\mathbf{q})$  is the configuration-dependent inertia matrix, and  $\boldsymbol{\tau}$  represents the sum of all non-contact forces, including inertial,

Coriolis, gravitational, and external forces. In the form of (7), it follows that  $\mathbf{Q} = \mathbf{M}(\mathbf{q})/h^2$  and  $\mathbf{b} = \mathbf{M}(\mathbf{q})\mathbf{v}/h + \boldsymbol{\tau}(\mathbf{q}, \mathbf{v})$ . As discussed in Section IV-E, the extended complementarity-free contact model (25) further incorporates a damping term with a diagonal damping matrix  $\mathbf{D}(\mathbf{q})$ .

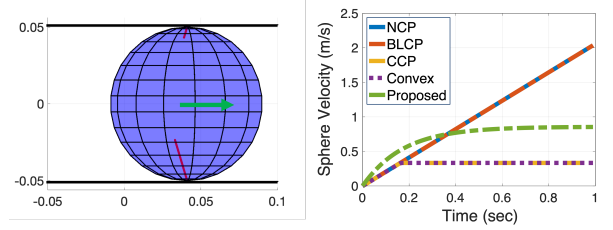


Fig. 4: Left: a sphere is accelerated between two frictional planes under an external force (green arrow). Right: the tangential velocity of the sphere versus time. NCP [29], [60] and BLCP [61] contact models capture the acceleration, while the velocity plateaus for the CCP [33] and Convex [23] models due to the "sheath effect" induced by the dual cone constraints. The proposed complementarity-free model mitigates such issue because it allows for "violation" of the dual cone constraints while also introducing significant smoothness.

1) *Setting 1: Sphere Sliding Between two Planes:* The task follows [60], which involves sliding a sphere between two parallel planes as depicted Fig. 4. The sphere with radius of 50 mm and mass 0.2kg begins at rest touching the lower plane. The top plane is 102mm above the bottom plane, so initially there is a gap of 2mm between the sphere and the top plane. The sphere is only given translational degrees of freedom and is accelerated with a constant force of 1N in the x-direction (shown in green arrow). The time step is 10ms, and the friction coefficient is 0.3. In the extended complementarity-free model (25), we set  $\mathbf{K}(\mathbf{q}) = 20\mathbf{I}$  and  $\mathbf{D}(\mathbf{q}) = 6\mathbf{I}$ . We compare the proposed (25) with NCP [29], [60], BLCP [61], CCP [33] and Convex [23] contact models. The results are shown in Fig. 4.

With an external force, the sphere is supposed to accelerate with only contact with the lower plane. NCP [29], [60] and BLCP [61] capture this. However, CCP [33] and Convex [23] models lead to the plateaus of velocity, so-called "sheath effect". This is because dual cone constraints in CCP and Convex models create the vertical motion of the sphere, leading to the contact force from the top plane (the red arrows in the left of Fig. 4 show the contact impulses). If the sphere needs to go faster, both planes need to move farther away. In contrast, because our proposed model (25) has relaxed the dual cone constraint, our model can effectively mitigate such effect: the plateau velocity of our model is higher than CCP/Convex. Fig. 4 also shows the softness of our model. This is expected because our generation of the contact force is handled as a spring-damper system (25) in the dual cone (Fig. 2(d)), which a smooth mapping (24) from system motion.

2) *Setting 2: Unactuated Cube Sliding with Initial Horizontal Velocity:* In this task, an unactuated cube with a mass of 0.01 kg, inertia of  $6 \times 10^{-6} \mathbf{I} \text{ kg}\cdot\text{m}^2$ , and size of 0.06 m slides on a frictional ground with an initial horizontal velocity of 2.0 m/s until it comes to rest, as shown in Fig. 5. The friction coefficient is set to 0.5, and the simulation time step is 2 ms. In the extended complementarity-free model (25), we use  $\mathbf{K}(\mathbf{q}) = \mathbf{I}$  and  $\mathbf{D}(\mathbf{q}) = 0.3\mathbf{I}$ . The baselines include the



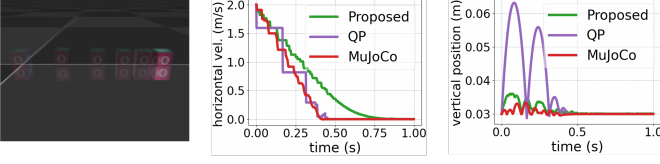


Fig. 5: Left: an unactuated box sliding with initial horizontal velocity. Middle and right: the horizontal velocity and vertical position trajectories, respectively. QP-based model (7) exhibits vertical motion artifacts due to the enforcement of dual cone constraints, the proposed model significantly mitigates these effects by relaxing the dual cone constraints. Compared to MuJoCo, our model yields noticeably smoother velocity profiles.

naive QP-based model (7) (in dynamic form) and the MuJoCo simulator [19]. Results are shown in the middle and right panels of Fig. 5. The vertical position trajectory (right) shows that the QP-based model (7) exhibits vertical motion artifacts due to the enforcement of the dual cone constraints, whereas the proposed model significantly mitigates these effects by relaxing the dual cone constraints. The horizontal velocity trajectory (middle plot) further demonstrates that, in comparison to MuJoCo, our model yields smoother behavior as a result of the soft handling of contact forces (24).

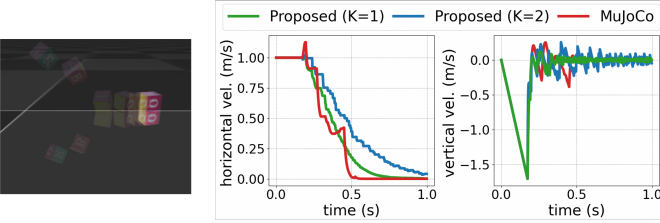


Fig. 6: Left: cube free falling, rolling, and sliding on ground. Middle and right: the horizontal and vertical velocity trajectories, respectively. Compared to MuJoCo, our model yields noticeably smoother velocity profiles. Increasing the stiffness  $K$  leads to increased oscillations in the contact resolution.

3) *Setting 3: Cube Free Falling, Rolling, and Sliding on Ground:* This task differs from Setting 2 only in the initial pose and velocity of the cube. Specifically, the initial position is  $[0.1, 0, 0.2]^\top$ , the quaternion  $[0.577, 0.577, 0.577, 0]^\top$ , the linear velocity  $[1.0, 0, 0]^\top$ , and the angular velocity  $[20, 0, 0]^\top$ . These initial conditions cause the cube to undergo free fall, followed by rolling and sliding on the ground until it comes to rest. We evaluate the extended complementarity-free model (25) using two different stiffness matrices:  $K(q) = I$  and  $K(q) = 2I$ , while keeping all other parameters identical to those in Setting 2. The baseline for comparison is the MuJoCo simulator. As shown in Fig. 6, the proposed model produces behavior similar to MuJoCo, but with noticeably smoother velocity profiles. Moreover, increasing the spring stiffness  $K$  leads to greater oscillations in the contact response, highlighting the importance of incorporating a damping term in (25) for stable and realistic contact behavior.

## VII. FINGERTIPS IN-AIR MANIPULATION

With the quasi-dynamic complementarity-free contact model (23), we evaluate the complementarity-free MPC (Algorithm

1) for three-fingertip manipulation tasks, comparing it to the MPC of the QP-based contact model (7). Hereafter, we refer to the latter as “Implicit MPC” since the QP-based model (7) needs to be converted into its KKT conditions in the MPC (26), similar to [43], [62], to order for the MPC optimization to be solved with existing tools [57]. All tasks below use MuJoCo as simulation environments. The proposed complementarity-free model (23) is only used in MPC for control optimization.

### A. Environment and Task Setup

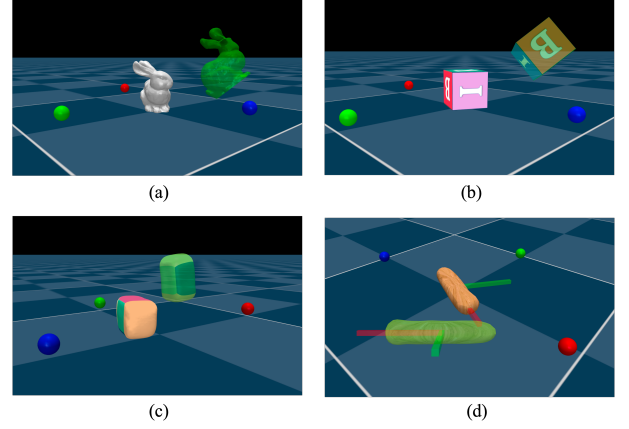


Fig. 7: Three-fingertip manipulation of different objects. Three fingertips (red, green, blue) are actuated. The tests include 4 objects: (a) Stanford bunny, (b) cube, (c) foam brick, and (d) stick. The transparent objects are the target poses. For visualization, we have attached a virtual frame to the stick to show its pose. The diameter of those objects ranges from 0.05[m] to 0.15[m].

The three-fingertips manipulation system is shown in Fig. 7. MuJoCo [19] is used for environment simulation. The three fingertips (red, green, and blue) are actuated with a low-level PD controller ( $K_p = 100$  and  $K_v = 2$ ) with gravity compensation. We use four different objects: Stanford bunny, cube, foambrick, and stick, all with mass of 0.01 [kg]. The diameter of those objects ranges from 0.08 [m] to 0.15 [m]. The initial pose of objects are statically lying on the ground with random xy position ( $x_0^{\text{obj}}, y_0^{\text{obj}}$ ) and random initial heading (yaw) angle  $\psi_0^{\text{obj}}$ , uniformly sampled as

$$x_0^{\text{obj}} \ y_0^{\text{obj}} \sim \mathcal{U}[-0.025, 0.025][\text{m}], \quad \psi_0^{\text{obj}} \sim \mathcal{U}[-\pi, \pi]. \quad (28)$$

We will consider three types of manipulation tasks:

- **On-ground rotation:** The target object pose is on the ground. The fingertips only need to move and rotate the object to align it with the target.
- **On-ground flipping:** The target requires flipping the object on the ground, with some target poses in non-equilibrium.
- **In-air manipulation:** The target pose is in the air. The fingertips must coordinate to prevent the object from falling while moving it to the target.

### B. MPC Setting and Results

To show the versatility of the proposed complementarity-free MPC, we use the same model parameters and MPC cost function for all tasks and objects. The model setting is in Table

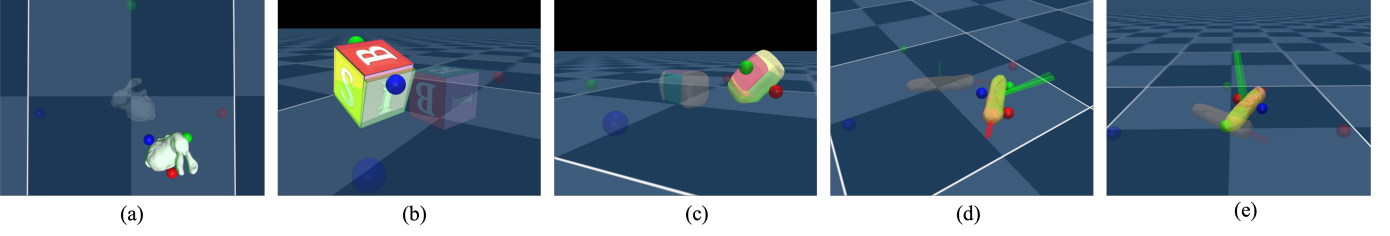


Fig. 8: On-ground manipulation examples. (a) On-ground rotation of Stanford bunny. (b) On-ground flipping of cube. (c) On-ground flipping of foambrick. (d)-(e) On-ground flipping of stick. In all figures, the initial object pose and fingertip positions are shown in transparency, and the final object pose and fingertip positions are shown in solid. The target object pose is coated with green. [Video link](#).

TABLE II: The model setting for all objects and tasks.

Name	Value
$\mathbf{q} \in \mathbb{R}^{7+9}$	object pose and 3D positions of three fingertips
$\mathbf{u} \in \mathbb{R}^9$	desired fingertip displacement, sent to low-level controller
$\mathbf{K}_r$	$K_p \mathbf{I}$ , $K_p=100$ is stiffness of fingertips' low-level control
$h$	0.1 [s]
$\epsilon \mathbf{M}_o / h^2$	diag(50, 50, 50, 0.05, 0.05, 0.05)
$\mathbf{K}(\mathbf{q})$	$\mathbf{I}$

II. The MPC path and final cost functions for all objects and tasks are defined as

$$c(\mathbf{q}, \mathbf{u}) := c_{\text{contact}}(\mathbf{q}) + 0.05c_{\text{grasp}}(\mathbf{q}) + 50 \|\mathbf{u}\|^2, \quad (29)$$

$$V(\mathbf{q}) := 5000 \|\mathbf{p}^{\text{obj}} - \mathbf{p}_{\text{target}}\|^2 + 50 (1 - (\mathbf{q}_{\text{target}}^T \mathbf{q}^{\text{obj}})^2)$$

Here, the final cost  $V(\mathbf{q})$  defines the “distance-to-goal” for the object’s position and quaternion<sup>1</sup>. In the path cost  $c(\mathbf{q}, \mathbf{u})$ , we define each term below. The contact cost term, defined as

$$c_{\text{contact}}(\mathbf{q}) := \sum_{i=1}^3 \|\mathbf{p}^{\text{obj}} - \mathbf{p}^{f_{t_i}}\|^2, \quad (30)$$

is to encourage the contact between fingertips (position  $\mathbf{p}^{f_{t_i}}$ ) and object (position  $\mathbf{p}^{\text{obj}}$ ). The grasp cost term, defined as

$$c_{\text{grasp}}(\mathbf{q}) := \|\tilde{\mathbf{p}}_{\text{obj}}^{f_{t_1}} + \tilde{\mathbf{p}}_{\text{obj}}^{f_{t_2}} + \tilde{\mathbf{p}}_{\text{obj}}^{f_{t_3}}\|^2, \quad (31)$$

is to encourage three fingertips to form a stable grasp shape. Here,  $\tilde{\mathbf{p}}_{\text{obj}}^{f_{t_i}}$  is the unit directional vector from the object position  $\mathbf{p}^{\text{obj}}$  to fingertip position  $\mathbf{p}^{f_{t_i}}$ , viewed in object frame  $R^{\text{obj}}$ :

$$\tilde{\mathbf{p}}_{\text{obj}}^{f_{t_i}} := (R^{\text{obj}})^T (\mathbf{p}^{f_{t_i}} - \mathbf{p}^{\text{obj}}) / \|\mathbf{p}^{f_{t_i}} - \mathbf{p}^{\text{obj}}\|. \quad (32)$$

This grasp cost is critical for in-air manipulation, where a stable grasp is essential to prevent dropping. The weights for each term in (29) are chosen based on the physical unit scale [6]. The control lower and upper bounds are  $\mathbf{u}_{\text{lb}} = -0.005$  and  $\mathbf{u}_{\text{ub}} = 0.005$ , and MPC prediction horizon is  $T = 4$ . In Implicit MPC, we set the complementarity relaxation factor to  $5 \times 10^{-4}$  for its best performance, while keeping all other parameters identical to those in the complementarity-free MPC.

We deem a manipulation task successful (and terminate the MPC rollout) if both of the following conditions are met:

$$\begin{aligned} \|\mathbf{p}^{\text{obj}} - \mathbf{p}_{\text{target}}\| &\leq 0.02 \text{ [m]}, \\ 1 - (\mathbf{q}_{\text{target}}^T \mathbf{q}^{\text{obj}})^2 &\leq 0.015, \end{aligned} \quad (33)$$

<sup>1</sup>The quaternion cost/error is defined as  $(1 - (\mathbf{q}_{\text{target}}^T \mathbf{q}^{\text{obj}})^2)$ , as used in [63]. The angle  $\theta$  between two normalized quaternions,  $\mathbf{q}_1$  and  $\mathbf{q}_2$ , is calculated as:  $\theta = \arccos(2(\mathbf{q}_1^T \mathbf{q}_2)^2 - 1)$ .

consecutively for 20 MPC rollout steps. A manipulation task is deemed a failure if the object does not satisfy (33) within the maximum MPC rollout length  $H = 2000$ .

1) *On-ground Rotation*: In on-ground rotation, the target object position  $\mathbf{p}_{\text{target}} = [x_{\text{target}}, y_{\text{target}}, z_{\text{height}}]^T$  is sampled as

$$x_{\text{target}} \text{ and } y_{\text{target}} \sim \mathcal{U}[-0.1, 0.1] \text{ [m]}, \quad (34)$$

and  $z_{\text{height}}$  is the height of the object lying on ground. The target object quaternion is  $\mathbf{q}_{\text{target}} = \text{rpyToQuat}(\phi_{\text{target}}, \theta_{\text{target}}, \psi_{\text{target}})$ , with yaw  $\psi_{\text{target}}$ , pitch  $\theta_{\text{target}}$ , and roll  $\phi_{\text{target}}$  sampled as

$$\psi_{\text{target}} \sim \mathcal{U}[-\pi, \pi], \quad \theta_{\text{target}} = \phi_{\text{target}} = 0. \quad (35)$$

For each object, we conduct 20 trials with different random initial and target poses. The results are given in Table III, where the manipulation accuracy is evaluated using

$$\begin{aligned} \text{final position error: } & \|\mathbf{p}^{\text{obj}} - \mathbf{q}_{\text{target}}\|, \\ \text{final heading angle error: } & |\psi_{\text{target}} - \psi^{\text{obj}}|, \end{aligned} \quad (36)$$

both calculated using the last 20 steps of a MPC rollout. Fig. 8(a) shows a manipulation example for the Stanford bunny.

2) *On-ground Flipping*: Here, the random target object position is sampled from (34), and the random target quaternion  $\mathbf{q}_{\text{target}} = \text{rpyToQuat}(\phi_{\text{target}}, \theta_{\text{target}}, \psi_{\text{target}})$  is sampled by

$$\psi_{\text{target}} \sim \mathcal{U}[-\pi, \pi], \theta_{\text{target}} \sim \mathcal{U}[-\frac{\pi}{2}, \frac{\pi}{2}], \psi_{\text{target}} \sim \mathcal{U}[-\frac{\pi}{2}, \frac{\pi}{2}]. \quad (37)$$

Note that some target poses are in non-equilibrium.

For each object, we conduct 20 trials with different random initial and target poses. The results are in Table IV, where we quantify the manipulation accuracy by

$$\begin{aligned} \text{final position error: } & \|\mathbf{p}^{\text{obj}} - \mathbf{q}_{\text{target}}\|, \\ \text{final quaternion error}^1 & 1 - (\mathbf{q}_{\text{target}}^T \mathbf{q}^{\text{obj}})^2, \end{aligned} \quad (38)$$

both calculated using the last 20 steps of a MPC rollout. Fig. 8 visualizes some random trials of on-ground flip manipulation.

3) *In-air Manipulation*: Here, we consider the target object pose in mid-air. Without ground support, the three fingertips must prevent the object from falling while moving it to a target pose. The in-air target object position  $\mathbf{p}_{\text{target}} = [x_{\text{target}}, y_{\text{target}}, z_{\text{target}}]^T$  is sampled as

$$\begin{aligned} x_{\text{target}}, y_{\text{target}} &\sim \mathcal{U}[-0.1, 0.1] \text{ [m]}, \\ z_{\text{target}} &\sim \mathcal{U}[0.03, 0.08] \text{ [m]}. \end{aligned} \quad (39)$$

The in-air target object orientation is

$$\mathbf{q}_{\text{target}} = \text{AxisAngleToQuat}(\mathbf{n}_{\text{target}}, \alpha_{\text{target}}), \quad (40)$$

TABLE III: Results for on-ground rotation manipulation

Object	Final position error (36)		Final heading angle error (36)		MPC solving time		Success rate	
	Implicit MPC	proposed	Implicit MPC	proposed	Implicit MPC	proposed	Implicit MPC	proposed
Stanford bunny	0.0146 [m] ± 0.0037	<b>0.0068 [m]</b> ± <b>0.0018</b>	0.153 [rad] ± 0.065	<b>0.0404 [rad]</b> ± <b>0.0215</b>	33 [ms]	<b>12 [ms]</b>	95%	<b>100%</b>
Cube	0.0116 [m] ± 0.0045	<b>0.0102 [m]</b> ± <b>0.0047</b>	0.0939 [rad] ± 0.0605	<b>0.0383 [rad]</b> ± <b>0.0154</b>	27 [ms]	<b>12 [ms]</b>	100%	<b>100%</b>
Foambrick	0.0137 [m] ± 0.0036	<b>0.0079 [m]</b> ± <b>0.0027</b>	0.0938 [rad] ± 0.0424	<b>0.0454 [rad]</b> ± <b>0.0287</b>	47 [ms]	<b>15 [ms]</b>	100%	<b>100%</b>

Results for each object are based on 20 random trials, each with random initial and target object poses. A trial is successful if conditions (33) are met **consecutively** for 20 MPC rollout steps. Final errors are computed using the last 20 rollout steps in successful trials.

TABLE IV: Results for on-ground flip manipulation

Object	Final position error (38)		Final quaternion error (38)		MPC solving time		Success rate	
	Implicit MPC	proposed	Implicit MPC	proposed	Implicit MPC	proposed	Implicit MPC	proposed
Cube	0.0309 [m] ± 0.0254	<b>0.0106 [m]</b> ± <b>0.0033</b>	0.1147 ± 0.1549	<b>0.0036</b> ± <b>0.0033</b>	31 [ms]	<b>12 [ms]</b>	20%	<b>100%</b>
Foambrick	0.0240 [m] ± 0.0169	<b>0.0101 [m]</b> ± <b>0.00322</b>	0.1389 ± 0.2004	<b>0.0036</b> ± <b>0.0020</b>	57 [ms]	<b>15 [ms]</b>	40%	<b>95%</b>
Stick	0.0118 [m] ± 0.0156	<b>0.0079 [m]</b> ± <b>0.0045</b>	0.0768 ± 0.198	<b>0.0053</b> ± <b>0.0023</b>	51 [ms]	<b>15 [ms]</b>	80%	<b>100%</b>

Each object's results are based on 20 random trials. For implicit MPC, final position or quaternion errors are computed using all trials due to fewer successful trials. For the proposed method, the errors are computed using successful trials.

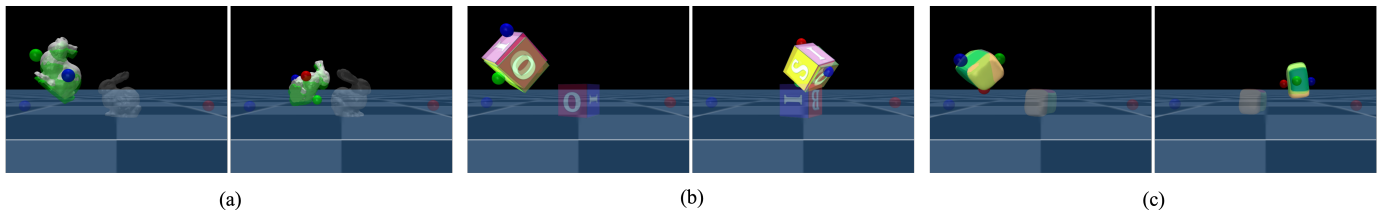


Fig. 9: In-air manipulation examples. (a) Two random trials of bunny in-air manipulation. (b) Two random trials of cube in-air manipulation. (c) Two random trials of foambrick in-air manipulation. In all examples, the initial object pose and fingertip positions are shown in transparency, and the final object pose and fingertips positions are in solid. The target object pose is coated in green. [Video link](#).

with random axis and angle sampled from

$$\mathbf{n}_{\text{target}} \sim \mathcal{N}([0 \ 1 \ 1]^T, 0.1\mathbf{I}), \quad \alpha_{\text{target}} \sim \mathcal{U}[-\pi, \pi]. \quad (41)$$

The results of in-air manipulation are listed in Table V. Due to the very low success rate of Implicit MPC for this task type, its results are not included. Manipulation accuracy is measured using the metrics in (38). Fig. 9 shows some random examples of in-air manipulation with different objects.

TABLE V: Results for in-air manipulation

Object	Final position error (38)	Final quaternion error (38)	MPC solving time	Success rate
Stanford bunny	0.0082 [m] ± 0.0021	0.0025 ± 0.0026	13 [ms]	90%
Cube	0.0093 [m] ± 0.0021	0.0029 ± 0.0024	13 [ms]	90%
Foambrick	0.0074 [m] ± 0.0016	0.0032 ± 0.0021	17 [ms]	95%

Each object's results are based on 20 trials, each with a random initial and target pose. A trial is considered successful if conditions (33) are met consecutively for 20 MPC rollout steps.

### C. Result Analysis

On results in Tables III-V, we make the following comments.

(1) The proposed complementarity-free MPC consistently outperforms Implicit MPC (i.e., MPC with complementarity model) across various manipulation tasks in terms of success rate, accuracy, and speed. The superiority is more evident in complex tasks like on-ground flipping and in-air manipulation.

(2) Quantitatively, the proposed complementarity-free MPC consistently achieves state-of-the-art results, with 100% success in on-ground rotation, over 95% in on-ground flipping, and over 90% in in-air manipulation. The average of the final object position error is 8.9 [mm] (noting object diameters range from 50 [mm] to 150 [mm]) and final quaternion error is 0.0035 (equivalent to 6.844°) across all tasks and objects. The MPC frequency consistently exceeds 58 Hz for all tasks.

(3) The above state-of-the-art results are largely due to the explicit, complementarity-free nature of the proposed contact model, which significantly improves the feasibility of contact optimization. In IPOPT solver, the complementarity-free MPC optimization usually converges to a solution within around 20 iterations. In contrast, Implicit MPC optimization struggles and



TABLE VI: The model settings for two dexterous manipulation environments

Name	TriFinger in-hand manipulation	Allegro hand on-palm reorientation
$\mathbf{q}$	$\mathbf{q} \in \mathbb{R}^{7+9}$ including object's 6D pose and TriFinger's 9 joints	$\mathbf{q} \in \mathbb{R}^{7+16}$ including object's 6D pose and all fingers' 16 joints
$\mathbf{u}$	$\mathbf{u} \in \mathbb{R}^9$ : desired finger joint displacement, sent to low-level control	$\mathbf{u} \in \mathbb{R}^{16}$ : desired finger joint displacement, sent to low-level control
$\mathbf{K}_r$	$K_p \mathbf{I}$ , $K_p = 10$ is the stiffness of fingers' low-level controller	$K_p \mathbf{I}$ , $K_p = 1$ is the stiffness of fingers' low-level controller
$h$	$h = 0.1$ [s]	
$\epsilon \mathbf{M}_o / h^2$	$\text{diag}(50, 50, 50, 0.1, 0.1, 0.1)$ for all objects	
$\mathbf{K}(\mathbf{q})$	$0.5 \mathbf{I}$ for all objects (chosen based on the results in Fig. 10)	

takes longer to converge due to the numerous complementarity constraints, even with relaxation.

#### D. How to Set the Model Parameter $\mathbf{K}$ ?

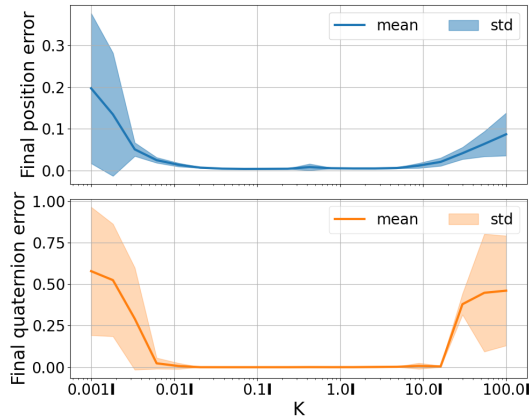


Fig. 10: Complementarity-free MPC performance with different parameter  $\mathbf{K}$  values for on-ground rotation tasks. Shaded areas are the standard deviation, computed from 10 random trials.

In the above implementation, model parameters (Table II) follow standard setting [52], except for the new stiffness matrix  $\mathbf{K}$ . We simply set  $\mathbf{K}$  as an identity matrix for all tasks. Now, we examine how different  $\mathbf{K}$  values affect MPC performance using the bunny on-ground rotation tasks. All parameters follow Table II, except  $\mathbf{K}$ , which varies from  $10^{-3} \mathbf{I}$  to  $10^2 \mathbf{I}$ . For each  $\mathbf{K}$ , we run 10 trials with different initial and target poses. MPC rollout length is 500. Fig. 10 shows the task performance versus different  $\mathbf{K}$ , where the final position and quaternion errors (38) are calculated at the last rollout step.

Fig. 10 shows that good performance is achieved across a wide range of  $\mathbf{K}$  settings, from  $0.01 \mathbf{I}$  to  $10 \mathbf{I}$ . Outside this range, MPC performance declines. This highlights the flexibility in choosing an effective  $\mathbf{K}$  value. Additionally, since the proposed complementarity-free model is fully differentiable, more complex  $\mathbf{K}(\mathbf{q})$  settings can be learned from environment data, which we plan to explore in future work.

### VIII. REAL-TIME DEXTEROUS IN-HAND MANIPULATION

With the quasi-dynamic complementarity-free contact model (23), the complementarity-free MPC is evaluated in dexterous in-hand manipulation tasks with two environments:

- **TriFinger in-hand manipulation.** As in Fig. 11(a), the three-fingered robotic hand faces down and each finger has

3 DoFs, actuated with low-level joint PD controllers with proportional gain  $K_p = 10$  and damping gain  $K_d = 0.05$ .

- **Allegro hand on-palm reorientation.** An Fig. 11(b), the four-fingered hand faces up and each finger has 4 DoFs. We implemented a low-level joint PD controller for each finger with control gains:  $K_p = 1$  and  $K_d = 0.05$ .

All tasks use MuJoCo as simulation environments. The proposed complementarity-free model (23) is only used in MPC for control optimization.

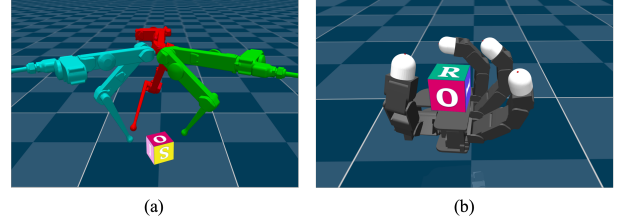


Fig. 11: (a) TriFinger in-hand manipulation. (b) 4-Fingered Allegro hand on-palm reorientation. Both simulation environments are built using MuJoCo [19].

In each environment, we focus on dexterous manipulation of 17 objects with diverse geometries, shown in Fig. 1. The object meshes are from the ContactDB dataset [64], with some proportional scaling to fit the workspace of the two hands. Object diameters range from 50 mm to 150 mm. In both environments, the goal is to manipulate objects from random initial poses to randomly given target poses. To show the versatility of our complementarity-free MPC, we use the same object-related parameters in our model across environments and objects, despite varying physical properties. The model settings are listed in Table VI.

#### A. TriFinger In-hand Manipulation

1) *Task Setup:* The TriFinger in-hand manipulation task involves moving various objects (the first row of Fig. 1) from a random on-ground initial pose ( $\mathbf{p}_0^{\text{obj}}, \mathbf{q}_0^{\text{obj}}$ ) to a given random on-ground target pose ( $\mathbf{p}_{\text{target}}, \mathbf{q}_{\text{target}}$ ). The initial object position  $\mathbf{p}_0^{\text{obj}} = [x_0^{\text{obj}}, y_0^{\text{obj}}, z_{\text{height}}^{\text{obj}}]$  is sampled as

$$x_0^{\text{obj}}, y_0^{\text{obj}} \sim \mathcal{U}[-0.05, 0.05] \text{ [m]}, \quad (42)$$

with  $z_{\text{height}}$  being the height of an object when it rests on ground. The initial object quaternion is  $\mathbf{q}_0^{\text{obj}} = \text{rpyToQuat}(\phi_0^{\text{obj}}, 0, 0)$ , with its heading (yaw)  $\phi_0^{\text{obj}}$  sampled from

$$\phi_0^{\text{obj}} \sim \mathcal{U}\left[-\frac{\pi}{2}, \frac{\pi}{2}\right] \text{ [rad]}. \quad (43)$$

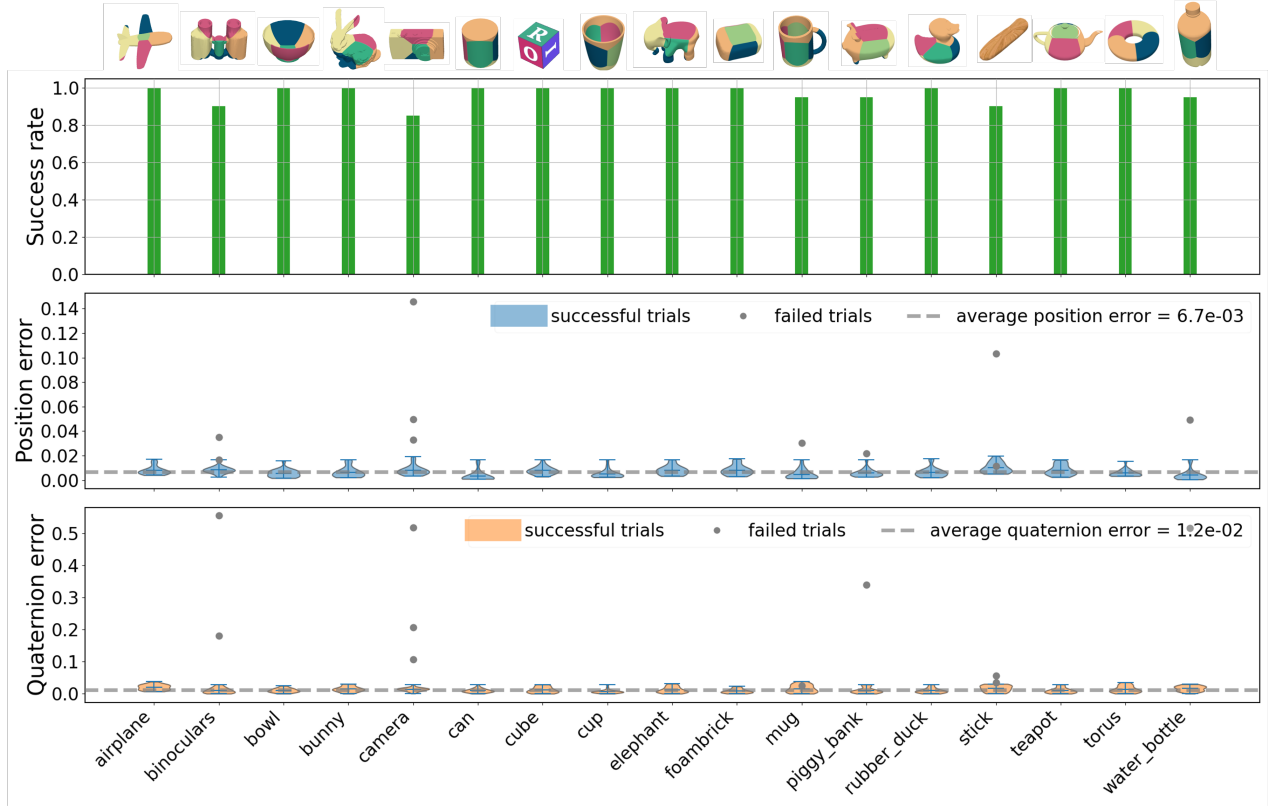


Fig. 12: Results of the TriFinger in-hand manipulation for various objects. For each object on the x-axis, the upper panel shows the success rate across 20 trials based on criterion (49). The middle and bottom panels show violin plots of the final position and quaternion errors in successful trials, with errors in failed trials indicated by gray dots. All errors are calculated according to (38). [Video link](#).

The target position  $\mathbf{p}_{\text{target}} = [x_{\text{target}}, y_{\text{target}}, z_{\text{height}}]$  is sampled as

$$x_{\text{target}}, y_{\text{target}} \sim \mathcal{U}[-0.05, 0.05] \text{ [m]}, \quad (44)$$

and the target object heading (yaw) is sampled from

$$\phi_{\text{target}} \sim \mathcal{U}\left[-\frac{\pi}{2}, \frac{\pi}{2}\right] \text{ [rad]}. \quad (45)$$

The above target range is set based on the reachable workspace of the TriFinger hand, consistent with [6].

In the complementarity-free MPC, the path and final cost functions are defined as

$$\begin{aligned} c(\mathbf{q}, \mathbf{u}) &:= c_{\text{contact}}(\mathbf{q}) + 0.05 c_{\text{grasp}}(\mathbf{q}) + 10 \|\mathbf{u}\|^2, \\ V(\mathbf{q}) &:= 5000 \|\mathbf{p}^{\text{obj}} - \mathbf{p}_{\text{target}}\|^2 + 50 (1 - (\mathbf{q}_{\text{target}}^T \mathbf{q}^{\text{obj}})^2), \end{aligned} \quad (46)$$

respectively. Here, the contact cost term  $c_{\text{contact}}$  is defined as the sum of squared distance between object and fingertip positions:

$$c_{\text{contact}}(\mathbf{q}) := \sum_{i=1}^3 \|\mathbf{p}^{\text{obj}} - \mathbb{FK}(\mathbf{q}^{\text{finger}_i})\|^2, \quad (47)$$

with  $\mathbb{FK}(\mathbf{q}^{\text{finger}_i})$  the forward kinematics of finger  $i$ ; other cost terms follow (29). The MPC control bounds are  $\mathbf{u}_{\text{lb}} = -0.01$  and  $\mathbf{u}_{\text{ub}} = 0.01$ . MPC prediction horizon is  $T = 4$ .

2) *Results*: For each object, we run the MPC policy for 20 trials. In each trial, we randomize the initial object and target poses according to (42)-(45). The MPC rollout length is set to  $H = 500$ . The rollout early terminates if both of the following conditions

$$\|\mathbf{p}^{\text{obj}} - \mathbf{p}_{\text{target}}\| \leq 0.02 \text{ [m]}, \quad 1 - (\mathbf{q}_{\text{target}}^T \mathbf{q}^{\text{obj}})^2 \leq 0.04, \quad (48)$$

are met consecutively for 20 rollout steps. We define

$$\text{a trial} \begin{cases} \text{succeeds,} & \text{if (48) is met consecutively for 20} \\ & \text{rollout steps within } H = 500, \\ \text{fails,} & \text{otherwise.} \end{cases} \quad (49)$$

Fig. 12 presents the TriFinger in-hand manipulation results, with the x-axis representing each object. The upper panel shows the success rate across 20 trials, while the middle and bottom panels respectively show violin plots of the final position and quaternion errors in successful trials, calculated according to (38). Errors in the failed trials are also shown in “gray dots”. The key performance metrics across all objects and all trials are summarized in Table VII.

TABLE VII: Summary of the TriFinger in-hand manipulation results across all objects and trials

Metric	Value
Overall success rate	97.0% $\pm$ 4.5%
Overall final position error <sup>a</sup> (38)	0.0067 $\pm$ 0.0041 [m]
Overall final quaternion error (38)	0.0124 $\pm$ 0.0090
Overall final angle error <sup>b</sup>	11.78° $\pm$ 5.10°
Average MPC solving time per rollout step	13 $\pm$ 3 [ms]

<sup>a</sup> Note that object diameters range from 50 [mm] to 150 [mm].

<sup>b</sup> The angle error is calculated by  $\theta = \arccos(2(\mathbf{q}_{\text{target}}^T \mathbf{q}^{\text{obj}})^2 - 1)$ .

3) *Analysis*: Fig. 12 and Table VII demonstrate that the proposed complementarity-free MPC consistently achieves high success rates and accuracy in TriFinger in-hand manipulation across diverse objects, with MPC running at around 80 Hz.

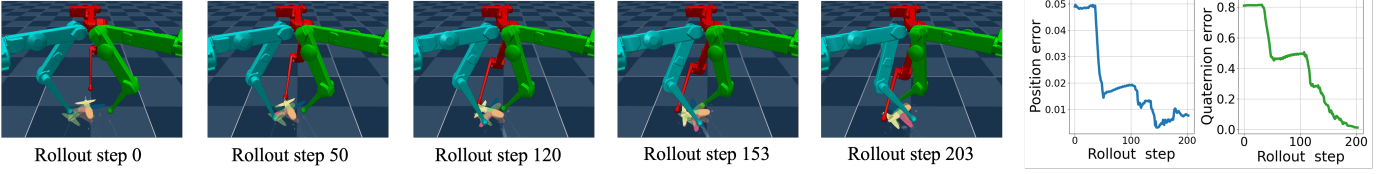


Fig. 13: An example of the TriFinger in-hand manipulation of an airplane object. The first five panels are screenshots of a MPC rollout at different steps, with the target shown in transparency. The final panel draws the position and quaternion errors (38) along the rollout steps.

These results represent state-of-the-art performance compared to the previous work [6]. Fig. 13 illustrates a MPC rollout example for in-hand manipulation of an airplane object.

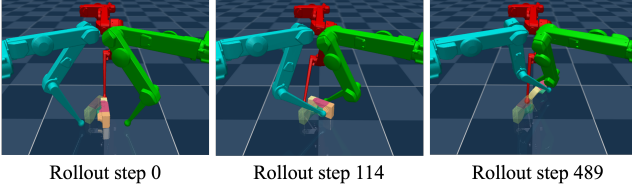


Fig. 14: An example of failed trial in manipulating camera.

Despite the high overall success rate, failures occur for few objects, e.g., camera (success rate 85%) and stick (success rate 90%). In Fig. 14, we show a failed trial. We observed that the primary cause of the manipulation failure was the self-collision of the three fingers. Since self-collision is not included as a motion constraint in our MPC optimization, it can occur when object pose approaches the edge of valid workspace.

### B. Allegro Hand On-palm Reorientation

1) *Task Setup*: The Allegro hand on-palm reorientation tasks involve reorienting various objects (Fig. 1) from a random initial pose  $(\mathbf{p}_0^{\text{obj}}, \mathbf{q}_0^{\text{obj}})$  to a randomly given target pose  $(\mathbf{p}_{\text{target}}, \mathbf{q}_{\text{target}})$ . The initial pose of an object rests on the hand palm, with the position  $\mathbf{p}_0^{\text{obj}}$  sampled from the palm center perturbed by a zero-mean Gaussian noise with standard deviation  $0.005\mathbf{I}$  [m]. The initial object orientation is  $\mathbf{q}_0^{\text{obj}} = \text{rpyToQuat}(\phi_0^{\text{obj}}, 0, 0)$ , with its heading (yaw) angle  $\phi_0^{\text{obj}}$  sampled from

$$\phi_0^{\text{obj}} \sim \mathcal{U}[-\frac{\pi}{2}, \frac{\pi}{2}] \text{ [rad]}. \quad (50)$$

To prevent the object from falling, we set the target object position at the center of the palm. The target orientation is  $\mathbf{q}_{\text{target}} = \text{rpyToQuat}(\phi_{\text{target}}, 0, 0)$ , with the heading (yaw) angle  $\phi_{\text{target}}$  sampled via

$$\phi_{\text{target}} \sim \phi_0^{\text{obj}} + \mathcal{U}(\{-\frac{\pi}{2}, \frac{\pi}{2}\}) \text{ [rad]}. \quad (51)$$

That is, the target orientation a rotation of the initial orientation  $\phi_0^{\text{obj}}$  by  $\pi/2$  or  $-\pi/2$  uniformly. We choose this large discrete target orientations instead of a continuous range to make the reorientation tasks more challenging for the Allegro hand.

The complementarity-free model setting is in Table VI. In MPC, the path and final cost functions are defined as

$$c(\mathbf{q}, \mathbf{u}) := c_{\text{contact}}(\mathbf{q}) + 0.1 \|\mathbf{u}\|^2 \\ V(\mathbf{q}) := 1000 \|\mathbf{p}^{\text{obj}} - \mathbf{p}_{\text{target}}\|^2 + 50 (1 - (\mathbf{q}_{\text{target}}^T \mathbf{q}^{\text{obj}})^2), \quad (52)$$

respectively. Here,  $c_{\text{contact}}$  is defined as the sum of the squared distance between object position and all fingertips:

$$c_{\text{contact}}(\mathbf{q}) := \sum_{i=1}^4 \|\mathbf{p}^{\text{obj}} - \mathbb{FK}(\mathbf{q}^{\text{finger}_i})\|^2, \quad (53)$$

with  $\mathbb{FK}(\mathbf{q}^{\text{finger}_i})$  the forward kinematics of finger  $i$ . Compared to (46), we remove the grasp cost term in  $c(\mathbf{q}, \mathbf{u})$  because we found including it is unnecessary for the Allegro hand tasks here. We also decrease the weight for the position cost in  $V(\mathbf{q})$  to prioritize the re-orientation accuracy instead of position. The control bounds for the Allegro hand are  $\mathbf{u}_{\text{lb}} = -0.2$  and  $\mathbf{u}_{\text{ub}} = 0.2$ . MPC prediction horizon is  $T=4$ .

2) *Results*: For each object (Fig. 1), we run the MPC policy for 20 trials, each with random initial and target poses. The MPC rollout length is set to  $H = 500$ , and the rollout is terminated early if the following condition,

$$1 - (\mathbf{q}_{\text{target}}^T \mathbf{q}^{\text{obj}})^2 \leq 0.04, \quad (54)$$

is met consecutively for 20 rollout steps. We define

$$\text{a trial} \begin{cases} \text{succeeds} & \text{if (54) is met for consecutive 20} \\ & \text{rollout steps within } H = 500, \\ \text{fails} & \text{otherwise.} \end{cases} \quad (55)$$

Fig. 15 presents the Allegro hand on-palm reorientation results for different objects. For each object (x-axis), the upper panel shows the success rate across 20 random trials, while the bottom panel show the violin plots of final quaternion errors in successful trials. Errors in failed trials are shown as “gray dots”. The final quaternion error is calculated using (38). Table VIII summarizes the overall performance.

TABLE VIII: Summary of the Allegro hand on-palm reorientation results over all objects and all trials

Metric	Value
Overall success rate	97.64% $\pm$ 5.18%
Overall final quaternion error	0.0116 $\pm$ 0.0088
Overall final angle error <sup>a</sup>	11.50° $\pm$ 4.61°
Average MPC solving time per rollout step	19 $\pm$ 3 [ms]

<sup>a</sup> Angle error is calculated by  $\theta = \arccos(2(\mathbf{q}_{\text{target}}^T \mathbf{q}^{\text{obj}})^2 - 1)$ .

3) *Analysis*: Fig. 15 and Table VIII demonstrate the state-of-the-art performance of the proposed complementarity-free MPC for Allegro hand on-palm reorientation. The overall success rate is 97.64%  $\pm$  5.18%, with an average reorientation error of 11.50°  $\pm$  4.61°, and MPC runs at over 50 Hz. Fig. 16 shows a MPC rollout example for stick reorientation.

Fig. 15 shows lower success rates for the airplane (90%) and stick (80%). The primary reason for these failures is the large



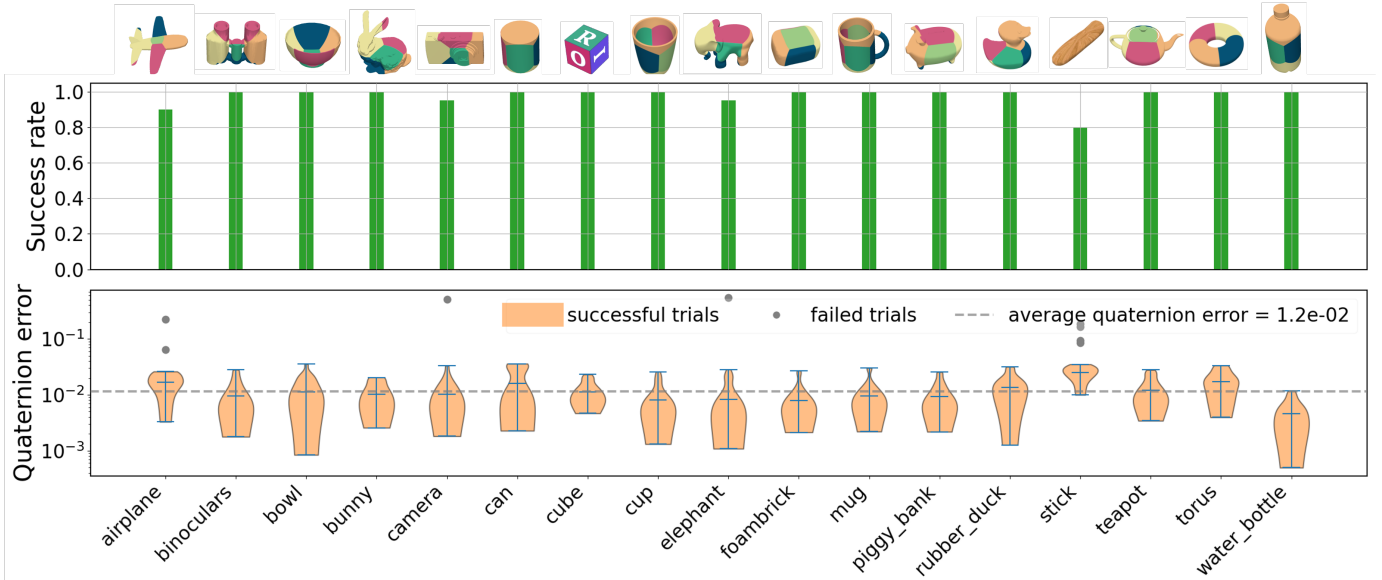


Fig. 15: Results of the Allegro hand on-palm reorientation of diverse objects. For each object (in x-axis), the upper panel shows the success rate across 20 random trials based on the criterion (55). The bottom panel shows the violin plots of quaternion errors (log-scale) in all successful trials. Here, errors in failed trials are shown as “gray dots”. The quaternion error is defined in (38). [Video link](#).

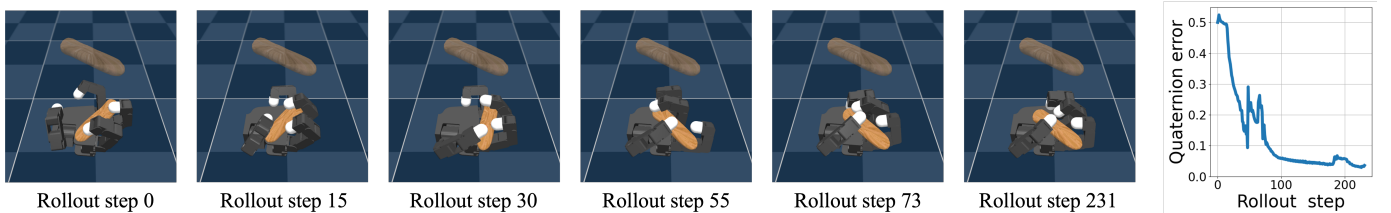


Fig. 16: An example of the Allegro hand reorientation of a stick object. The first six images display the screenshots of a MPC rollout at different steps, with the target orientation shown in transparency. The last column shows the quaternion error (38) along rollout steps.

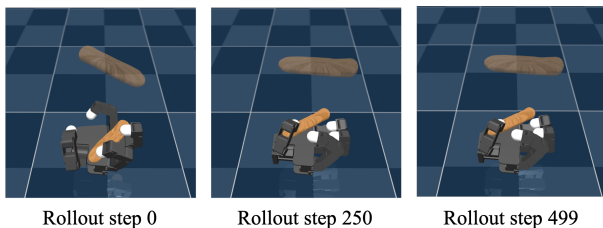


Fig. 17: A failure case for stick reorientation.

object geometry relative to the Allegro palm, causing those objects to become out of reach or stuck between the fingers during reorientation. Fig. 17 gives a failure case.

### C. Limitation and Future Work

In our experiments, we found the contact-implicit MPC is limited to handle dexterous manipulation that requires contact reasoning over *global* geometry. In Algorithm 1, our contact-implicit MPC optimization relies on a fixed and locally linearized geometry (Jacobian). This means the MPC optimizes contact plans using local linearized geometry. Thus, it may struggle with tasks requiring global contact optimization. For example, in peg-in-hole tasks, successfully inserting asymmetrical objects into slots requires global contact reasoning.

To address this limitation, one potential direction is to integrate a collision detection pipeline directly into the MPC optimization. However, this approach can pose computational challenges, as collision detection itself can be a non-differentiable optimization problem. Our recent work [65], which introduces an end-to-end smooth contact model encompassing both collision detection and time stepping, may offer a promising solution. Another direction involves incorporating a high-level geometric planner to guide the contact-implicit MPC. Among these directions, the proposed complementarity-free multi-contact model remains a strong candidate for efficient and scalable local contact reasoning. We plan to explore these research directions in future work.

### IX. CONCLUSION

We propose a complementarity-free multi-contact model for planning and control in dexterous manipulation. By reformulating complementarity constructs into closed forms within the duality of optimization-based contact formulations, our model offers significant computational benefits in contact-rich modeling and optimization: time-stepping explicitness, automatic sanctification with Coulomb friction law, differentiability, and fewer hyperparameters. The effectiveness of the proposed complementarity-free model and its MPC have been thoroughly

evaluated in a range of challenging dexterous manipulation tasks, including fingertips in-air 3D manipulation, TriFinger in-hand manipulation, and Allegro hand on-palm reorientation, all involving diverse objects. The results show that our method consistently achieves state-of-the-art results for highly versatile, high-accuracy, and real-time contact-rich dexterity.

## APPENDIX

### A. Proof of Lemma 1

The KKT optimality condition of the optimization (12) writes

$$\frac{1}{h^2} (\tilde{\mathbf{J}}\mathbf{Q}^{-1}\tilde{\mathbf{J}}^\top + \mathbf{R})\boldsymbol{\beta} + \frac{1}{h} (\tilde{\mathbf{J}}\mathbf{Q}^{-1}\mathbf{b} + \tilde{\boldsymbol{\phi}}) - \boldsymbol{\mu} = \mathbf{0}, \quad (56)$$

$$\mathbf{0} \leq \boldsymbol{\mu} \perp \boldsymbol{\beta} \geq \mathbf{0},$$

with  $\boldsymbol{\mu}$  the vector of the Lagrangian multipliers for the constraints in (12). Writing  $\boldsymbol{\mu}$  in terms of  $\boldsymbol{\beta}$  from the first equation and substituting it the second equation leads to (1), which completes the proof.

### B. Proof of Lemma 2

With a positive definite diagonal matrix  $\mathbf{K}(\mathbf{q})$  replacing  $(\tilde{\mathbf{J}}\mathbf{Q}^{-1}\tilde{\mathbf{J}}^\top + \mathbf{R})^{-1}$  in (13), the approximation dual solution  $\boldsymbol{\beta}^+$  to (13) can be obtained based on the following identity

$$0 \leq x \perp x + \lambda \geq 0 \Leftrightarrow x = \max(-\lambda, 0), \quad (57)$$

which leads to (15). With the approximation dual solution (15), the approximation primal solution  $\mathbf{v}^+$  in (16) can be obtained by substituting  $\boldsymbol{\beta}^+$  to (11). This completes the proof.

## REFERENCES

- [1] OpenAI: Marcin Andrychowicz, Bowen Baker, Maciek Chociej, Rafal Jozefowicz, Bob McGrew, Jakub Pachocki, Arthur Petron, Matthias Plappert, Glenn Powell, Alex Ray, et al. Learning dexterous in-hand manipulation. *The International Journal of Robotics Research*, 39(1):3–20, 2020.
- [2] Aravind Rajeswaran, Vikash Kumar, Abhishek Gupta, Giulia Vezzani, John Schulman, Emanuel Todorov, and Sergey Levine. Learning complex dexterous manipulation with deep reinforcement learning and demonstrations. *arXiv preprint arXiv:1709.10087*, 2017.
- [3] Arthur Allshire, Mayank Mittal, Varun Lodaya, Viktor Makoviychuk, Denys Makoviichuk, Felix Widmaier, Manuel Wüthrich, Stefan Bauer, Ankur Handa, and Animesh Garg. Transferring dexterous manipulation from gpu simulation to a remote real-world trifinger. In *2022 IEEE/RSJ International Conference on Intelligent Robots and Systems (IROS)*, pages 11802–11809. IEEE, 2022.
- [4] Tao Chen, Jie Xu, and Pulkit Agrawal. A system for general in-hand object re-orientation. In *Conference on Robot Learning*, pages 297–307. PMLR, 2022.
- [5] Tao Pang, HJ Terry Suh, Lujie Yang, and Russ Tedrake. Global planning for contact-rich manipulation via local smoothing of quasi-dynamic contact models. *IEEE Transactions on Robotics*, 2023.
- [6] Wanxin Jin and Michael Posa. Task-driven hybrid model reduction for dexterous manipulation. *IEEE Transactions on Robotics*, 2024.
- [7] Samuel Pfrommer, Mathew Halm, and Michael Posa. Contactnets: Learning discontinuous contact dynamics with smooth, implicit representations. In *Conference on Robot Learning*, pages 2279–2291. PMLR, 2021.
- [8] Xianyi Cheng, Eric Huang, Yifan Hou, and Matthew T Mason. Contact motion guided motion planning for quasidynamic dexterous manipulation in 3d. In *2022 International Conference on Robotics and Automation (ICRA)*, pages 2730–2736. IEEE, 2022.
- [9] Wanxin Jin, Alp Aydinoglu, Mathew Halm, and Michael Posa. Learning linear complementarity systems. In *Learning for Dynamics and Control Conference*, pages 1137–1149. PMLR, 2022.
- [10] Taylor A Howell, Simon Le Cleac’h, Jan Brüdigam, J Zico Kolter, Mac Schwager, and Zachary Manchester. Dojo: A differentiable physics engine for robotics. *arXiv preprint arXiv:2203.00806*, 2022.
- [11] Hyung Ju Terry Suh, Tao Pang, and Russ Tedrake. Bundled gradients through contact via randomized smoothing. *IEEE Robotics and Automation Letters*, 7(2):4000–4007, 2022.
- [12] Shenao Zhang, Wanxin Jin, and Zhaoran Wang. Adaptive barrier smoothing for first-order policy gradient with contact dynamics. In *International Conference on Machine Learning*, pages 41219–41243. PMLR, 2023.
- [13] Alp Aydinoglu and Michael Posa. Real-time multi-contact model predictive control via admm. In *2022 International Conference on Robotics and Automation (ICRA)*, pages 3414–3421. IEEE, 2022.
- [14] William Yang and Michael Posa. Dynamic on-palm manipulation via controlled sliding. *arXiv preprint arXiv:2405.08731*, 2024.
- [15] Vince Kurtz, Alejandro Castro, Aykut Özgün Önel, and Hai Lin. Inverse dynamics trajectory optimization for contact-implicit model predictive control. *arXiv preprint arXiv:2309.01813*, 2023.
- [16] Simon Le Cleac’h, Taylor A Howell, Shuo Yang, Chi-Yen Lee, John Zhang, Arun Bishop, Mac Schwager, and Zachary Manchester. Fast contact-implicit model predictive control. *IEEE Transactions on Robotics*, 2024.
- [17] Anusha Nagabandi, Kurt Konolige, Sergey Levine, and Vikash Kumar. Deep dynamics models for learning dexterous manipulation. In *Conference on Robot Learning*, pages 1101–1112. PMLR, 2020.
- [18] Erwin Coumans and Yunfei Bai. Pybullet, a python module for physics simulation for games, robotics and machine learning. <http://pybullet.org>, 2016–2023.
- [19] Emanuel Todorov, Tom Erez, and Yuval Tassa. Mujoco: A physics engine for model-based control. In *2012 IEEE/RSJ International Conference on Intelligent Robots and Systems*, pages 5026–5033. IEEE, 2012.
- [20] Russ Tedrake and the Drake Development Team. Drake: Model-based design and verification for robotics, 2019.
- [21] Jeongseok Lee, Michael X. Grey, Sehoon Ha, Tobias Kunz, Sumit Jain, Yuting Ye, Siddhartha S. Srinivasa, Mike Stilman, and C Karen Liu. Dart: Dynamic animation and robotics toolkit. *The Journal of Open Source Software*, 3(22):500, 2018.
- [22] Alessandro Tasora, Radu Serban, Hammad Mazhar, Arman Pazouki, Daniel Melanz, Jonathan Fleischmann, Michael Taylor, Hiroyuki Sugiyama, and Dan Negrut. Chrono: An open source multi-physics dynamics engine. In *High Performance Computing in Science and Engineering: Second International Conference, HPCSE 2015, Solná, Czech Republic, May 25–28, 2015, Revised Selected Papers 2*, pages 19–49. Springer, 2016.
- [23] Mihai Anitescu. Optimization-based simulation of nonsmooth rigid multibody dynamics. *Mathematical Programming*, 105:113–143, 2006.
- [24] David Stewart and Jeffrey C Trinkle. An implicit time-stepping scheme for rigid body dynamics with coulomb friction. In *Proceedings 2000 ICRA. Millennium Conference. IEEE International Conference on Robotics and Automation. Symposia Proceedings (Cat. No. 00CH37065)*, volume 1, pages 162–169. IEEE, 2000.
- [25] Moritz Geilinger, David Hahn, Jonas Zehnder, Moritz Bäcker, Bernhard Thomaszewski, and Stelian Coros. Add: Analytically differentiable dynamics for multi-body systems with frictional contact. *ACM Transactions on Graphics (TOG)*, 39(6):1–15, 2020.
- [26] Xueyi Liu, Kangbo Lyu, Jieqiong Zhang, Tao Du, and Li Yi. Quasisim: Parameterized quasi-physical simulators for dexterous manipulations transfer. *arXiv preprint arXiv:2404.07988*, 2024.
- [27] Yuval Tassa, Tom Erez, and Emanuel Todorov. Synthesis and stabilization of complex behaviors through online trajectory optimization. In *2012 IEEE/RSJ International Conference on Intelligent Robots and Systems*, pages 4906–4913. IEEE, 2012.
- [28] Iordanis Chatzinikolaïdis, Yangwei You, and Zhibin Li. Contact-implicit trajectory optimization using an analytically solvable contact model for locomotion on variable ground. *IEEE Robotics and Automation Letters*, 5(4):6357–6364, 2020.
- [29] David E Stewart. Rigid-body dynamics with friction and impact. *SIAM review*, 42(1):3–39, 2000.
- [30] David E Stewart and Jeffrey C Trinkle. An implicit time-stepping scheme for rigid body dynamics with inelastic collisions and coulomb friction. *International Journal for Numerical Methods in Engineering*, 39(15):2673–2691, 1996.
- [31] David E Stewart. Convergence of a time-stepping scheme for rigid-body dynamics and resolution of painlevé’s problem. *Archive for Rational Mechanics and Analysis*, 145:215–260, 1998.
- [32] Steven P Dirkse and Michael C Ferris. The path solver: a nonmonotone stabilization scheme for mixed complementarity problems. *Optimization methods and software*, 5(2):123–156, 1995.

- [33] Mihai Anitescu and Alessandro Tasora. An iterative approach for cone complementarity problems for nonsmooth dynamics. *Computational Optimization and Applications*, 47:207–235, 2010.
- [34] Alessandro Tasora and Mihai Anitescu. A matrix-free cone complementarity approach for solving large-scale, nonsmooth, rigid body dynamics. *Computer Methods in Applied Mechanics and Engineering*, 200(5-8):439–453, 2011.
- [35] Tao Pang and Russ Tedrake. A convex quasistatic time-stepping scheme for rigid multibody systems with contact and friction. In *2021 IEEE International Conference on Robotics and Automation (ICRA)*, pages 6614–6620. IEEE, 2021.
- [36] Wanxin Jin, Shaoshuai Mou, and George J Pappas. Safe pontryagin differentiable programming. *Advances in Neural Information Processing Systems*, 34:16034–16050, 2021.
- [37] Emanuel Todorov. Implicit nonlinear complementarity: A new approach to contact dynamics. In *2010 IEEE international conference on robotics and automation*, pages 2322–2329. IEEE, 2010.
- [38] Katsu Yamane and Yoshihiko Nakamura. Stable penalty-based model of frictional contacts. In *Proceedings 2006 IEEE International Conference on Robotics and Automation, 2006. ICRA 2006.*, pages 1904–1909. IEEE, 2006.
- [39] Walter Rudin et al. *Principles of mathematical analysis*, volume 3. McGraw-hill New York, 1964.
- [40] Jean-Pierre Sleiman, Farbod Farshidian, Maria Vittoria Minniti, and Marco Hutter. A unified mpc framework for whole-body dynamic locomotion and manipulation. *IEEE Robotics and Automation Letters*, 6(3):4688–4695, 2021.
- [41] Carlos Mastalli, Rohan Budhiraja, Wolfgang Merkt, Guilhem Saurel, Bilal Hammoud, Maximilien Naveau, Justin Carpentier, Ludovic Righetti, Sethu Vijayakumar, and Nicolas Mansard. Crocodyl: An efficient and versatile framework for multi-contact optimal control. In *IEEE International Conference on Robotics and Automation*, pages 2536–2542. IEEE, 2020.
- [42] Alexander W Winkler, C Dario Bellicoso, Marco Hutter, and Jonas Buchli. Gait and trajectory optimization for legged systems through phase-based end-effector parameterization. *IEEE Robotics and Automation Letters*, 3(3):1560–1567, 2018.
- [43] Michael Posa, Cecilia Cantu, and Russ Tedrake. A direct method for trajectory optimization of rigid bodies through contact. *The International Journal of Robotics Research*, 33(1):69–81, 2014.
- [44] Igor Mordatch, Emanuel Todorov, and Zoran Popović. Discovery of complex behaviors through contact-invariant optimization. *ACM Transactions on Graphics (ToG)*, 31(4):1–8, 2012.
- [45] Alp Aydinoglu, Adam Wei, Wei-Cheng Huang, and Michael Posa. Consensus complementarity control for multi-contact mpc. *arXiv preprint arXiv:2304.11259*, 2023.
- [46] Bernardo Aceituno-Cabezas and Alberto Rodriguez. A global quasi-dynamic model for contact-trajectory optimization in manipulation. In *Robotics: Science and Systems Foundation*, 2020.
- [47] Wei-Cheng Huang, Alp Aydinoglu, Wanxin Jin, and Michael Posa. Adaptive contact-implicit model predictive control with online residual learning. In *2024 IEEE International Conference on Robotics and Automation (ICRA)*, pages 5822–5828. IEEE, 2024.
- [48] Weiwei Li and Emanuel Todorov. Iterative linear quadratic regulator design for nonlinear biological movement systems. In *First International Conference on Informatics in Control, Automation and Robotics*, volume 2, pages 222–229. SciTePress, 2004.
- [49] Joel A E Andersson, Joris Gillis, Greg Horn, James B Rawlings, and Moritz Diehl. CasADi – A software framework for nonlinear optimization and optimal control. *Mathematical Programming Computation*, 11(1):1–36, 2019.
- [50] Haozhi Qi, Ashish Kumar, Roberto Calandra, Yi Ma, and Jitendra Malik. In-hand object rotation via rapid motor adaptation. In *Conference on Robot Learning*, pages 1722–1732. PMLR, 2023.
- [51] Matthew T Mason. *Mechanics of robotic manipulation*. MIT press, 2001.
- [52] Tao Pang, H. J. Terry Suh, Lujie Yang, and Russ Tedrake. Planning for contact-rich manipulation via local smoothing of quasi-dynamic contact models. *IEEE Transactions on Robotics*, 39(6):4691–4711, 2023.
- [53] Neville Hogan. Impedance control: An approach to manipulation. In *1984 American control conference*, pages 304–313. IEEE, 1984.
- [54] Jia Pan, Sachin Chitta, and Dinesh Manocha. Fcl: A general purpose library for collision and proximity queries. In *2012 IEEE International Conference on Robotics and Automation*, pages 3859–3866. IEEE, 2012.
- [55] Stephen Boyd and Lieven Vandenbergh. *Convex optimization*. Cambridge university press, 2004.
- [56] Daniel Fiser. libccd, 2018.
- [57] Joel AE Andersson, Joris Gillis, Greg Horn, James B Rawlings, and Moritz Diehl. Casadi: a software framework for nonlinear optimization and optimal control. *Mathematical Programming Computation*, 11:1–36, 2019.
- [58] Andreas Wächter and Lorenz T Biegler. On the implementation of an interior-point filter line-search algorithm for large-scale nonlinear programming. *Mathematical programming*, 106:25–57, 2006.
- [59] Bartolomeo Stellato, Goran Banjac, Paul Goulart, Alberto Bemporad, and Stephen Boyd. Osqp: An operator splitting solver for quadratic programs. *Mathematical Programming Computation*, 12(4):637–672, 2020.
- [60] Peter C Horak and Jeff C Trinkle. On the similarities and differences among contact models in robot simulation. *IEEE Robotics and Automation Letters*, 4(2):493–499, 2019.
- [61] Kenny Erleben. Velocity-based shock propagation for multibody dynamics animation. *ACM Transactions on Graphics (TOG)*, 26(2):12–es, 2007.
- [62] Taylor A Howell, Simon Le Cleac’h, Sumeet Singh, Pete Florence, Zachary Manchester, and Vikas Sindhwani. Trajectory optimization with optimization-based dynamics. *IEEE Robotics and Automation Letters*, 7(3):6750–6757, 2022.
- [63] Du Q Huynh. Metrics for 3d rotations: Comparison and analysis. *Journal of Mathematical Imaging and Vision*, 35:155–164, 2009.
- [64] Samarth Brahmabhatt, Cusuh Ham, Charles C Kemp, and James Hays. Contactdb: Analyzing and predicting grasp contact via thermal imaging. In *Proceedings of the IEEE/CVF conference on computer vision and pattern recognition*, pages 8709–8719, 2019.
- [65] Wen Yang and Wanxin Jin. Contactsdf: Signed distance functions as multi-contact models for dexterous manipulation. *IEEE Robotics and Automation Letters*, 10(5), 2025.